Science AAAS

Revised Manuscript

Femtosecond X-ray diffraction reveals a liquid-liquid phase transition in phase-change materials

Authors: P. Zalden[1,2,3,*], F. Quirin[4], M. Schumacher[5], J. Siegel[7], S. Wei[6], A. Koc[4,8], M. Nicoul[4], M. Trigo[1,2], P. Andreasson[9], H. Enquist[9], M. Shu[10], T. Pardini[11], M. Chollet[12], D. Zhu[12], H. Lemke[12], I. Ronneberger[5], J. Larsson[9], A. M. Lindenberg[1,2,14], H. E. Fischer[13], S. Hau-Riege[11], D. A. Reis[1,2], R. Mazzarello[5], M. Wuttig[6,15] and K. Sokolowski-Tinten[4,*]

Affiliations:

[1] Stanford PULSE Institute, SLAC National Accelerator Laboratory, 2575 Sand Hill Rd., CA 94025 Menlo Park, USA.

[2] Stanford Institute for Materials and Energy Sciences, SLAC National Accelerator Laboratory, 2575 Sand Hill Rd., CA 94025 Menlo Park, USA.

[3] European XFEL, Holzkoppel 4, 22869 Schenefeld, Germany.

[4] Faculty of Physics and Center for Nanointegration Duisburg-Essen (CENIDE), University of Duisburg-Essen, Lotharstrasse 1, 47048 Duisburg, Germany.

[5] Institut für Theoretische Festkörperphysik, JARA-FIT and JARA-HPC, RWTH Aachen University, Germany.

[6] I. Physikalisches Institut and JARA-FIT, RWTH Aachen, Sommerfeldstrasse 14, 52074 Aachen, Germany.

[7] Instituto de Optica, CSIC, C/Serrano 121, 28006 Madrid, Spain.

[8] Institut für Physik und Astronomie, Universität Potsdam, Karl-Liebknecht-Strasse 24-25, 14476 Potsdam, Germany.

[9] Department of Physics, Lund University, Professorsgatan 1, 223 62 Lund, Sweden.

[10] Department of Applied Physics, Stanford University, CA 94305 Stanford, USA.

[11] Lawrence Livermore National Laboratory, Livermore, CA, USA.

[12] Linac Coherent Light Source, SLAC National Accelerator Laboratory, 2575 Sand Hill Rd., CA 94025 Menlo Park, USA.

[13] Institut Laue-Langevin, 71 avenue des Martyrs, CS 20156, 38042 Grenoble cedex 9, France.

[14] Department of Materials Science and Engineering, Stanford University, CA 94305, Stanford, USA.

[15] PGI 10 (Green IT), Forschungszentrum Jülich, 52428 Jülich, Germany.

*Correspondence to: klaus.sokolowski-tinten@uni-due.de or peter.zalden@xfel.eu

Abstract: In phase-change memory devices, a material is cycled between glassy and crystalline states. The highly temperature-dependent kinetics of its crystallization process enable application in memory technology, but the transition has not been resolved on an atomic scale. Using femtosecond X-ray diffraction and ab initio computer simulations, we determine the time-dependent pair correlation function of phase-change materials throughout the melt-quenching and crystallization process. We found a liquid-liquid phase transition in the phase-change materials $Ag_4In_3Sb_{67}Te_{26}$ and $Ge_{15}Sb_{85}$ at 660 and 610 K, respectively. The transition is predominantly caused by the onset of Peierls-distortions, whose amplitude correlates with an increase of the apparent activation energy of diffusivity. This reveals a relationship between atomic structure and kinetics, enabling a systematic optimization of the memory switching kinetics.

One Sentence Summary: The onset of a Peierls-distortion in supercooled liquid phase-change materials enhances the kinetic contrast required for data storage.

Main Text: The global amount of data grows exponentially(*1*). Alternative memory technologies are considered to satisfy the resulting demands. Phase-change memory promises higher storage densities as well as faster retrieval rates due to the non-destructive read-out as compared to state-of-the-art memory technology(*2–5*). In phase-change memory, information storage occurs by cycling small volumes of the material between its glassy and crystalline states. An optically or electrically induced thermal stimulus allows switching between them. Crystallization is the time-limiting step as glass formation (vitrification) can be facilitated rapidly by a melt-quenching process. Nevertheless, even crystallization can take place within less than a nanosecond(*6–8*). Phase-change memory therefore relies on the kinetic contrast of the active materials: A high atomic mobility at elevated temperature allows quick crystallization, while low atomic mobility at ambient temperatures allows long-term data retention(*7*, *9–13*). Good glass forming materials are generally characterized by a glass transition temperature T_g, which is relatively close to the melting temperature T_m. This occurs for values of the Turnbull parameter $T_g/T_m \geq 2/3$ (*14*). Bad glass formers have typical values of $T_g/T_m \leq 1/2$, which enables rapid crystallization. Optimum performance of a phase-change material (PCM) cannot be achieved by focusing on any one of these criteria and the temperature dependence of atomic mobility, i.e., its viscosity, must be understood in detail to enable a systematic optimization of kinetic properties suitable for phase-change memory devices.

The temperature dependence of viscosity differs among various glass forming liquids as the temperature approaches the glass transition T_g. While some liquids show an Arrhenius-like behavior and are classified as “strong” (e.g. silica), others display a range of non-Arrhenius behaviors and are classified as “fragile” (e.g. o-terphenyl)(*15*). In some anomalous liquids, a fragile-to-strong (FTS) crossover may occur, where the high-temperature fragile liquid is transformed into a low-temperature strong liquid(*16–18*). The FTS crossover is usually associated with a maximum in thermodynamic response functions (e.g. heat capacity C_p, thermal expansivity α_P, and compressibility κ_T), which may be attributed to a phase transition between two liquid phases characterized by distinct physical properties (e.g. density and entropy) and different atomic structures. The FTS crossover was first proposed to explain the behavior of water, which is a fragile liquid down to the temperature of the homogeneous nucleation limit but behaves kinetically strong when heated from the solid amorphous state above T_g(*19*). Similar observations were made on the phase-change material (PCM) Ag-In-Sb-Te in its liquid and solid amorphous states(*9*, *12*, *20*). However, in PCMs, liquid quenching is difficult due to the rapid

onset of crystallization. This limits the accessible supercooling range at common cooling rates(*21*), making observations of FTS crossovers or liquid-liquid phase transitions (LLPT) difficult. The apparent FTS crossover in PCMs renders the hypothesis of LLPTs appealing, and also implies anomalous structural, thermodynamic and diffusive properties(*21–23*).

The microscopic mechanism underlying the crossover is unclear. Liquid $Ge_{15}Te_{85}$ shows an increase of medium range order (MRO) upon supercooling, compatible with an increase of local atomic distortions(*24*). Yet, $Ge_{15}Te_{85}$ is a good glass former and thus cannot be utilized as PCM. More generally, direct experimental evidence for LLPTs in systems that crystallize rapidly is rare, since the timescales available to probe the supercooled liquid state before it crystallizes are short - hence the name "no-man's land" was invented to refer to the highly supercooled region (150-236 K)(*25*) in the phase diagram of water, the nature of whose anomalies has long been debated(*26*). Only recently, ultrafast x-ray laser scattering has enabled directly probing supercooled water down to 227 K and revealed evidence of a continuous LLPT(*27*). From the computational side, LLPTs were observed previously in simulations of ST2 water(*28*, *29*), although the possibility of the existence of a true liquid-liquid critical point (LLCP) in the supercooled liquid has been challenged theoretically(*30*). In case of PCMs, similar data are not yet available, but an anomalous breakdown of the Stokes-Einstein relationship (SER) in the equilibrium liquid of $GeSb_2Te_4$ was recently observed and was speculated to be caused by a LLPT below T_m(*31*). We focused our attention on Sb-based PCMs, because $Ag_4In_3Sb_{67}Te_{26}$ (AIST)(*9*, *12*, *20*) and Ge_9Sb_{91}(*32*) have crossovers in the apparent activation energy of viscosity. Both materials are employed as PCMs in optical (AIST(*4*)) and electronic ($Ge_{15}Sb_{85}$(*33*)) memory devices.

The liquid-liquid phase-transition

We employed hard X-ray laser pulses from an X-ray free electron laser (the Linear Coherent Light Source, LCLS) to overcome the temporal limitation of probing the atomic structure of highly supercooled PCMs. At the X-ray Pump-Probe (XPP) instrument(*34*), optical laser pulses with 800 nm center wavelength and 50 fs pulse duration are absorbed by a thin film of PCM at time t_0. Subsequently, electron-phonon coupling heats the PCM on the few picosecond timescale(*35*, *36*), leading to melting at sufficiently high excitation fluences. The PCM is quenched by diffusive thermal transport into the supporting membrane of Si_3N_4, which is of similar thickness as the PCM. To probe the atomic structure during this melt-quench cycle, we collected the diffraction patterns of X-ray pulses with 1.305 Å center wavelength on a 2D area detector (Fig. S1(*37*)). We varied the delay Δt between the optical pump event at t_0 and the X-ray probe event at time t, $\Delta t = t - t_0$, between negative values and tens of microseconds. We performed each set of pump-probe events on a new spot of the sample, which was irreversibly modified due to the intense optical and X-ray pulses. Nevertheless, the X-ray probe pulse duration of 50 fs is sufficiently short to ensure that the atomic structure does not change during the probe interaction.

We found that the structure factor (S(q)) of amorphous AIST was dominated by two broad diffraction rings centered at $q_1 = 2.07(1)$ Å^{-1} and $q_2 = 3.21(2)$ Å^{-1}, clearly visible in Figs. 1A, B&D). At $\Delta t < 0$, the diffraction of the unpumped, as-deposited amorphous structure is recorded at the initial temperature of 298 K. At Δt of a few picoseconds, the peak intensity of both rings decreases, and their radii approach each other. Consistently, the ratio q_2/q_1 depicted in Fig. 1F) decreases within the first picoseconds, but almost recovers to the initial value of the amorphous state after a few nanoseconds. This behavior is strong evidence for a structural

transition in a disordered state beyond just a thermally induced reduction of the scattering efficiency (Debye-Waller), which would leave the peak positions unaffected. Further evidence for a phase transition behavior comes from the highly non-linear scaling of the peak structural modification with the pump fluence (Fig. 1G). The fact that crystallization eventually occurs at fluences above 14 mJ/cm^2 (see Fig. S4) enables us to derive a lower bound for the temperature jump several µs after optical excitation. At the time of crystallization (5 µs), the temperature in the PCM must be above the temperature where crystallization sets in at calorimetric heating rates of a few degrees Kelvin per minute. In AIST, this temperature is 430 K(*38*). A comparison with literature data on AIST (vertical grey lines) shows good agreement of the momentum transfer associated with the strongest reflections (Fig. 1E).

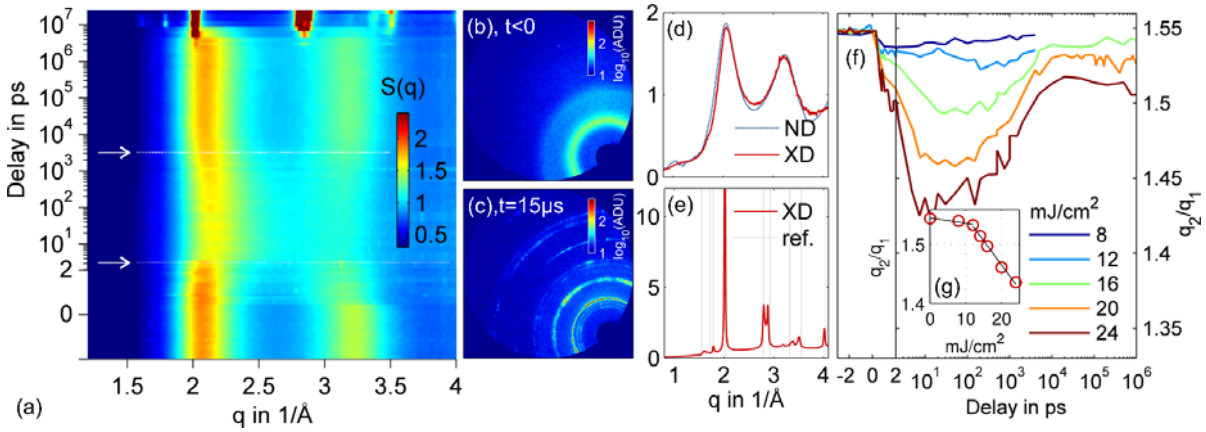

To quantify the temperature evolution of our samples more accurately, we performed finite element simulations. They allow associating temperatures to the structural information we obtained at various time delays and fluences. We show the resulting cooling behavior of the 50 nm thick film of AIST on 50 nm thick membranes (red curves) based on the normalized temperature $\Theta = \frac{T-T_0}{T_m-T_0}$, where T_m is the melting temperature, 810 K for AIST(*39*) and 860 K for $Ge_{15}Sb_{85}$(*40*) and T_0 the initial temperature of 298 K (Fig. 2). Following the heating by electron-phonon coupling, the heat diffuses from the PCM into the Si_3N_4 membrane after a few hundreds of picoseconds. Their temperature equilibrates after a few nanoseconds. Subsequently, thermal transport into the frame supporting the membranes becomes the dominant cooling mechanism. The experimental data (Fig. 1F) reflect the impact of the two different length scales of thermal transport associated with the short out-of-plane and the long in-plane axes. The timescale of out-of-plane transport is in good agreement with the change of atomic structure in the disordered state at around one nanosecond. We observed in-plane thermal transport only after delays longer than ten microseconds, rendering it irrelevant for this work. We derived two temporal intervals ($\{t_a\}$ and $\{t_b\}$, indicated in Fig. 2), independent of the pump fluence, over which the temperature of the PCM was stable within 10%. During these intervals, we can predict the temperature of the PCM most accurately, since it depends predominantly on the specific heat of the materials involved. We found the same intervals for 60 nm thick $Ge_{15}Sb_{85}$ films on 150 nm thick membranes.

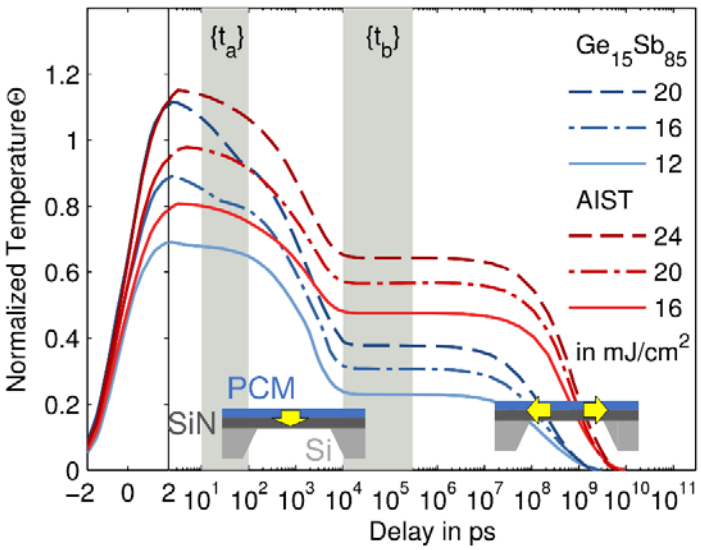

The atomic structure during $\{t_a\}$ and $\{t_b\}$ is described by the radii of the first (r_1) and second (r_2) coordination shells. We determined them from the pair correlation functions g(r) (Fig. 3A). They reveal a pronounced increase of r_1 upon excitation. The ratio $R = r_2/r_1$ provides information about the structural ordering and we measured the evolution with time and fluence (Figs. 3B, C).

Based on these numbers and in combination with the thermal simulations we determined R for AIST and $Ge_{15}Sb_{85}$ as a function of inverse temperature T_m/T (Fig. 4A). For each fluence of the pump laser, we derive one value of R from the intervals $\{t_a\}$ and $\{t_b\}$. Additionally, we derived one average value from the data at negative delays. Direct evidence for a structural transition in the supercooled liquids of AIST and $Ge_{15}Sb_{85}$ comes from a change in slope of $R=r_2/r_1$ in the range of T_m/T between 1 and 1.5. This resembles the r_2/r_1 behavior in the good glass former $Ge_{15}Te_{85}$ that also has a FTS crossover and a structural phase transition that correlate(*24*), albeit at higher temperatures. We interpolated our data with an error function that allowed us to determine the temperature of the structural transition by the maximum slope in r_2/r_1 occurring at 660±20 K and 610±20 K for AIST and $Ge_{15}Sb_{85}$, respectively. We estimate the experimental uncertainty as ±20K SD in our experiment mostly caused by statistical fluctuations in the pump fluence. A normalized version of the same error function fits the pre-peak intensity I_{pp} (Fig. 4B) in S(q), which was located at q=1.08±0.02 and 1.06±0.02 $Å^{-1}$ for AIST and $Ge_{15}Sb_{85}$, respectively. They correspond to the formation of periodic structures in real space with 5.8 and 5.9 Å, which is twice the radius of the first coordination shell r_1. The periodicity is due to the formation of alternating long and short bonds on opposite sides of a central atom, which is a characteristic fingerprint of a Peierls distortion(*41*). The resulting distortion pattern forces a pronounced reduction of g(r) around the second coordination shell due to its sensitivity to the broadening of the distribution of bond angles. The temperature dependence of R and I_{pp} matches the temperature dependence of the apparent activation energy of inverse diffusivity D^{-1} (Fig. 4C), which corresponds to the apparent activation energy of viscosity η assuming the SER is valid.

$$E_A = k_B \frac{\partial \log(D_0/D)}{\partial(1/T)}.$$

We derived the diffusivities (Fig. 4D) from previous measurements of the viscosity above T_m for AIST(*42*) and $Ge_{15}Te_{85}$(*43*). In case of AIST, we also calculated them from the crystal growth velocity in the supercooled liquid state(*12*). Due to the uncertainty regarding the validity of the SER in the supercooled regime we prefer to provide diffusivity data, which unlike viscosity data can be directly calculated from crystal growth velocities(*9*) and require the assumption of a valid SER only for the equilibrium liquid.

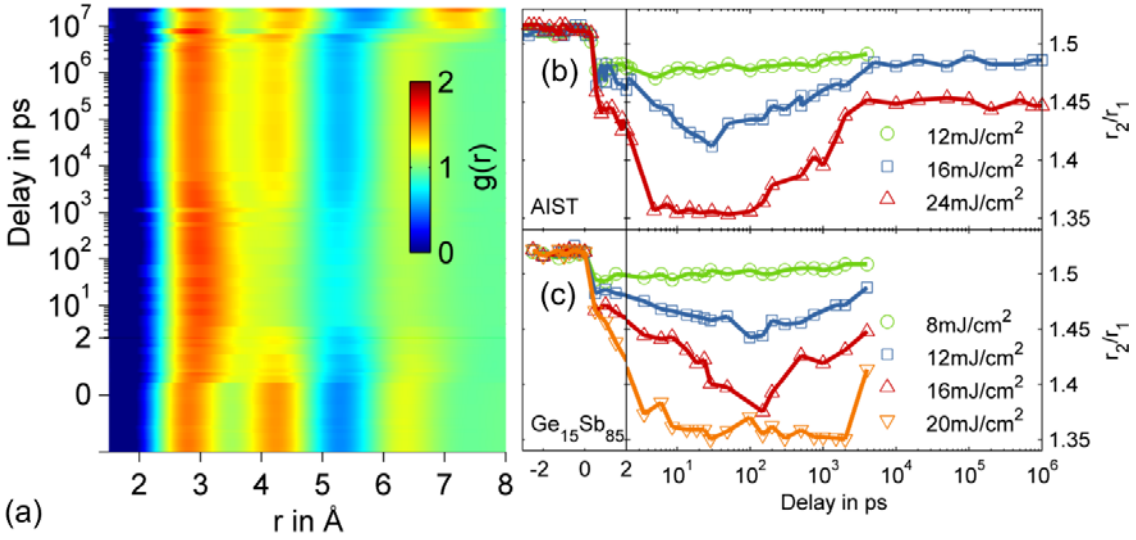

Two different temperatures characterize the transition process in R and I_{pp}: The inflection point and the onset temperature, where the first deviation from the low-temperature state occurs upon heating. This definition resulted from earlier observations of the onset of a non-Arrhenius scaling of viscosity upon heating – the FTS crossover. It was reported as 570 K in case of AIST and in the vicinity of the melting temperature in $Ge_{15}Te_{85}$. It coincides with the temperature, where in our measurements the atomic structure reaches ~90% of R for the low-temperature state in case of AIST and $Ge_{15}Te_{85}$. This temperature can be equally considered as onset of a structural transition in a hypothetical heating experiment. In $Ge_{15}Sb_{85}$, it occurs at a temperature of 550±20 K and at the melting point of 648 K in case of $Ge_{15}Te_{85}$. The inflection points on the other hand correspond to the LLPT, which is indicated as dotted vertical lines in Fig. 4 and occurs when the kinetic activation energy reaches about ~20% of its low temperature value. In the non-PCM $Ge_{15}Te_{85}$, it occurs at $T_{LL}/T_m = 1.05$(*24*, *44*), while the LLPT of the PCMs AIST and $Ge_{15}Sb_{85}$ takes place at $T_{LL}/T_m = 0.81\pm0.01$ and 0.71 ± 0.01, respectively.

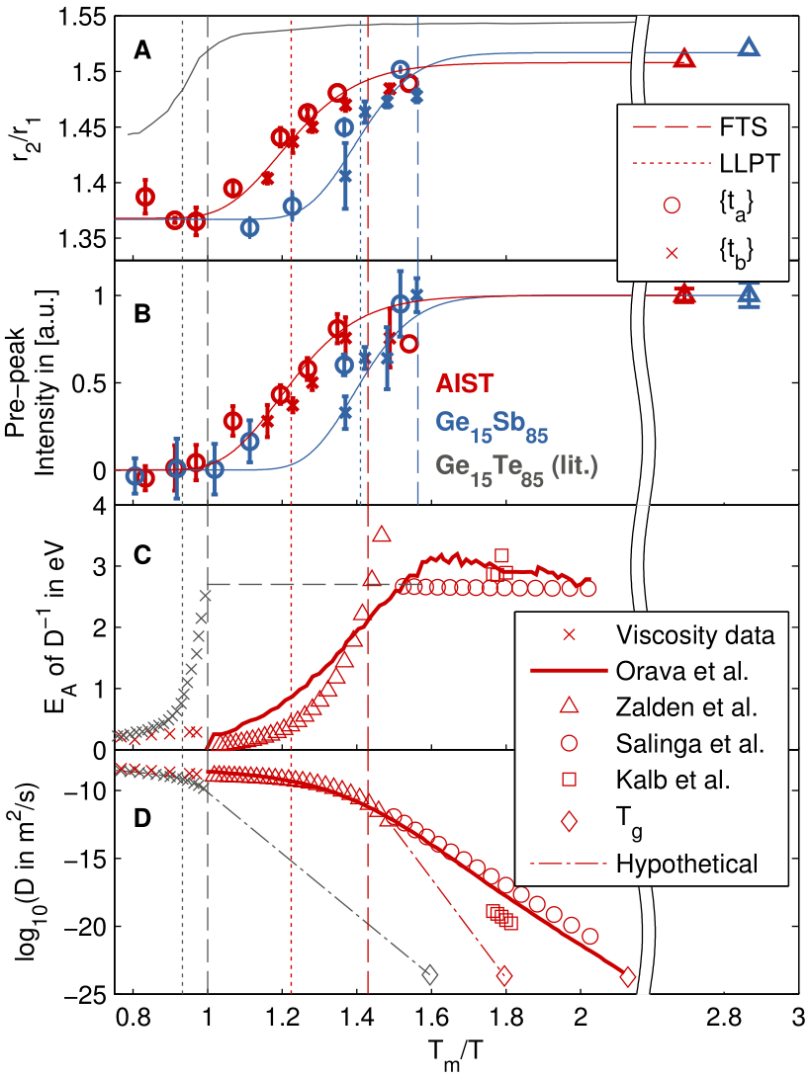

The role of the glass transition in the FTS crossover is still a matter of debate and leads to the question whether the PCMs below the crossover are in a supercooled liquid or glassy state. Orava et al. reported a strong liquid state of AIST based on T_g=378 K for a standard cooling rate of 20 K/min(*20*). The kinetic data underlying this scenario, however, agree with data reported by Salinga et al.(*9*) for the glass (Fig. 4D). In an alternative scenario, where the glass transition for similar standard rates is located at 450 K(*45*), the diffusivity of the strong liquid is hypothetically represented by an Arrhenius behavior (Fig. 4D) – similar to the case of $Ge_{15}Te_{85}$. To show that the structural transition at T_{LL} involves two liquid states, we need to show that the glass transition occurs at lower temperature. Given the reported glass transition of AIST at 450 K(*45*) for calorimetric heating rates of around 1 K/s, an enormous cooling rate dependence of T_g is required to explain a transition at 660 K. This requirement, however, is in contradiction with the invariant transition temperatures observed during the out-of-plane cooling during $\{t_a\}$ with 10^{11} K/s cooling rate and the in-plane cooling during $\{t_b\}$ with 10^6 K/s (Fig. S5c). The structural transition observed here therefore is a LLPT at temperature T_{LL}.

Microscopic nature of the transition

Liquid PCMs are commonly found to be octahedrally coordinated(*46*), but their corresponding amorphous states contain several competing structural motifs. (i) Local Peierls-distortions of an octahedral environment cause the splitting of the first coordination shell into two sub-shells with unequal occupation of the first and second sub-shells(*47*). While the Peierls-distortion itself leaves the R-parameter almost unchanged, the lower occupation of the second (larger) sub-shell will reduce r_1 and thereby increase R. This makes it impossible to distinguish this motif from an increase caused by the formation of (ii) tetrahedral sites, possibly together with (iii) homopolar bonds as reported for GeTe(*48*, *49*). Therefore, we require further information on the local structure to resolve the exact mechanism responsible for the LLPT. We performed ab initio molecular dynamics (AIMD) simulations and verified the simulations by comparing with the temperature dependent structure factors (Fig. S6). We reproduced with our simulations the peak shift and the reduction of intensity. We found R was less temperature dependent, which we attributed to the faster quench rate in the simulation ($3*10^{12}$ K/s) (*13*). At higher quenching rates, the liquid falls out of equilibrium at higher temperatures, kinetically freezing-in an intermediate state. The lack of equilibration time at each temperature step means the LLPT occurs over a wider temperature range. Nevertheless, the trend observed in AIMD was consistent with our experimental findings.

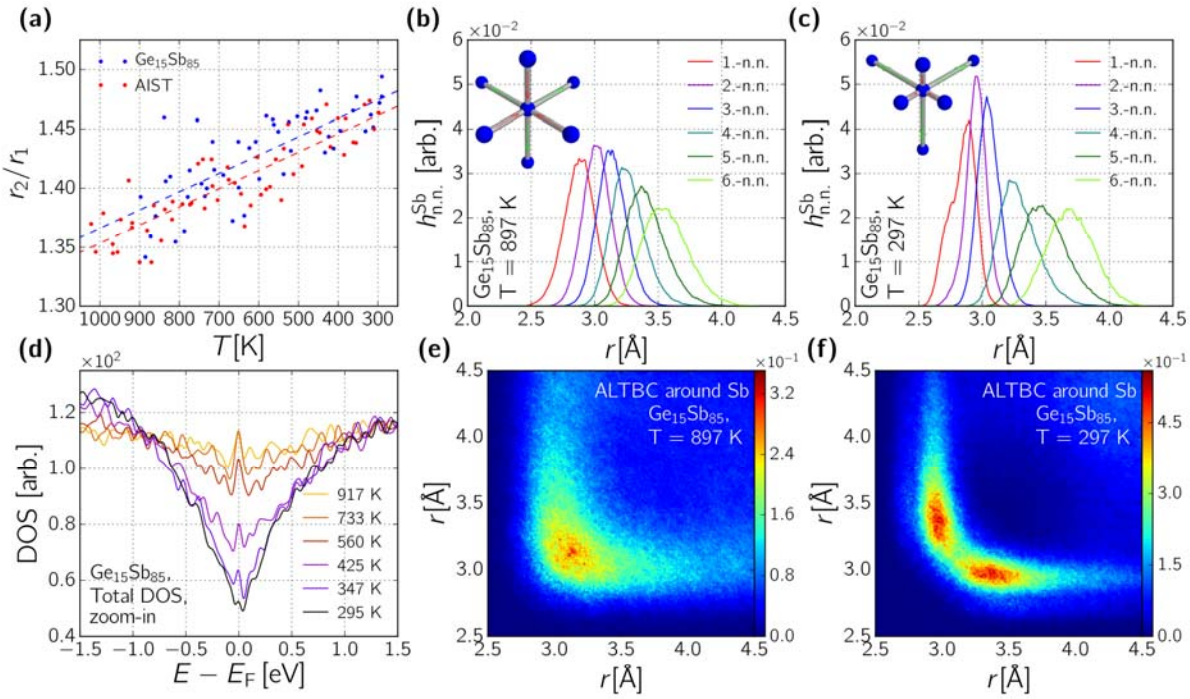

In case of $Ge_{15}Sb_{85}$, 70% of the total number of bonds were formed between Sb atoms, which dominated the local order and the scattering signal due to their higher atomic weight. Histograms of interatomic distances from a Sb atom to its n-th nearest Sb neighbor provide further insight. As Sb commonly is 6-fold coordinated, the histograms reflect the inner structure within the first coordination shell. In the liquid state (Fig. 5B), all six histograms have equidistant peaks of similar width, indicating a regular octahedral environment with regular fluctuations due to the dynamics in the liquid state. After quenching (Fig. 5C), the n=1-3 histograms shift to shorter distances, becoming narrower and higher. The n=4-6 histograms get separated further and retain their width from the liquid state. This different behavior between the three shorter and three

longer interatomic distances is evidence for the onset of a Peierls-distortion, also evident from the angular limited bond correlation (ALTBC) plots (Figs. 5E, F). The large variation of first-neighbor distances limits the discussion of R to a qualitative level, since the sixth-nearest neighbor distance in low-temperature $Ge_{15}Sb_{85}$ (Fig. 5c) is centered at 3.7 Å, which is closer to the center of mass for the second coordination shell (r_2 = 4.2 Å) than the first (r_1 = 2.9 Å). This means that the first and second coordination shells can no longer be resolved due to the inherent disorder. While the Peierls-distortion alone can explain the increase in R, the bond angles around Ge change from the octahedral value of 90° in the liquid state to a value of 105° at ambient conditions (Fig. S14). This indicates the formation of tetrahedral sites (R=1.61 for a purely tetrahedral structure), which also increase R. The conditions in AIST are comparable, but tetrahedral sites are formed during the quench only around a fraction of the 4% stoichiometric In atoms(*13*). Because AIST shows the same structural trend during the quench (Fig. 5A), a Peierls-distortion must be the dominant mechanism responsible for the change in kinetic properties. With increasing Peierls-distortion in supercooled liquid $Ge_{15}Sb_{85}$ and AIST we also observed a tendency of a pseudogap(*50*) opening in the density of states (Fig. 5D). Supercooled liquids $Ge_{15}Te_{85}$(*51*), As_2Se_3(*52*) and As_2Te_3(*53*) indeed undergo a metal-semiconductor transition during the quench, accompanied by a maximum of the thermodynamic response functions (e.g. C_p, α_P, and k_T), indicative of a fragile-to-strong crossover. Also the pseudogap of liquid $Ge_2Sb_2Te_5$ exhibits an opening tendency during the quench, suggesting that it might also show a LLPT in the supercooled liquid regime(*54*).

Discussion and Conclusion

We combine our observations and modelling to derive information on the change of the bonding mechanism underlying the LLPT. In the equilibrium liquid state, the metallic bonds are non-directional with a relatively low activation energy of viscosity. The formation of Peierls-distortions during the quench localizes electronic charge between the atoms, constraining bond angles and increasing the activation energy of viscosity. The tendency to form a Peierls-distortion in the crystalline state is in fact one of the characteristic attributes of PCMs, which are classified as incipient metals due to the sensitivity of their electronic localization on the distortion amplitude(*55*, *56*).

In conclusion, ultrafast X-ray diffraction after short pulse excitation provides access to the atomic structure of PCMs over the entire melt-quench cycle without interference of crystallization. The resulting diffraction data reveal a structural LLPT in AIST and $Ge_{15}Sb_{85}$. We used AIMD simulations to show that this LLPT in both PCMs is dominated by the formation of a Peierls-distortion, forming distinct short and long bonds and opening a pseudogap in the electronic density of states. Our observation is consistent with earlier predictions that the atomic energy gain by a Peierls-distortion $\Delta E_p < k_B T_m$(*57*), since we show that the distortion is formed at T_{LL}, which implies $\Delta E_p \approx k_B T_{LL}$. The temperature-dependent structural parameters correlate with the apparent activation energy of viscosity, which suggests that the LLPT is responsible for the FTS crossover previously reported in AIST. The kinetic transition associated with the FTS crossover has important implications for the application of PCMs in memory devices: The low kinetic activation energy of the high-temperature liquid ensures that the high atomic mobility of the equilibrium liquid is available for crystallization, i.e. for temperatures between T_m and T_{LL}. At temperatures below the LLPT, the Peierls-distortion localizes charge and stabilizes the amorphous atomic structure, which increases the kinetic activation energy and rapidly reduces the atomic mobility during the quench – enabling the formation of a stable glass at ambient

conditions. A material with lower T_{LL}/T_m therefore offers a wider temperature window between T_{LL} and T_m, where fast crystallization is possible and explains why AIST and $Ge_{15}Sb_{85}$ are PCMs, while $Ge_{15}Te_{85}$ is not. Our results offer a new strategy for the design of improved PCMs for specialized memory applications – based on the atomic bonding mechanism in these materials.

Figure captions

Fig. 1. Evolution of the atomic structure of AIST during the melt-quench, resolved in reciprocal space. (A) We show the structure factor S(q) of AIST after optical excitation with 24 mJ/cm^2 throughout the entire melt-quench cycle from the initial as-deposited amorphous state **(B)** to the final crystalline state **(C)**. The atomic structure factors of the initial and final states are in good agreement with reference data from total neutron scattering (ND) and literature values for the crystalline structure **(D&E)**. Femtosecond X-ray diffraction enables resolving an intermediate structural phase transition in the disordered state of AIST, as seen by the change in the ratio q_2/q_1 corresponding to a shift of reflections after few picoseconds and again after few nanoseconds **(F)**. The fluence dependence of the average q_2/q_1 after 10 to 100 ps shows an onset of the phase transition at 12 mJ/cm^2 **(G)**, indicated also in panel (A) by white horizontal arrows.

Fig. 2. Temporal evolution of the average temperature inside AIST (red curves) and $Ge_{15}Sb_{85}$ (blue curves) for different optical excitation conditions. We identified two intervals (grey areas), one between 10 and 100 ps $\{t_a\}$ and the other between 10 and 30 ns $\{t_b\}$, during which the temperature is stable within 10%. These time scales are associated with two thermal transport conditions, schematically depicted as insets (yellow arrows denote the main direction of heat flow) and are caused by the high aspect ratio of the samples.

Fig. 3. The average local structure in AIST and $Ge_{15}Sb_{85}$ during the melt-quench. (A) shows the atomic pair correlation functions g(r) of AIST as a function of time after optical excitation with 24 mJ/cm^2. The structural transition is most clearly evidenced by a transient shift of the first coordination shell r_1 to longer distances between ≈1 ps and ≈5 ns, much before the onset of crystallization ≈5 µs. Consequently, the structural parameter r_2/r_1 for AIST **(B)** and $Ge_{15}Sb_{85}$ **(C)** decreases and stays at the high-temperature value of 1.36 for several nanoseconds when the fluence is sufficiently high. In case crystallization is avoided at low pump fluences below 14.5 mJ/cm^2, r_2/r_1 eventually returns to its initial values (1.51±0.01 in case of AIST) in the final amorphous solid state, when ambient temperature is restored.

Fig. 4. The structural parameter $R=r_2/r_1$ (A), the intensity of a pre-peak (B) and the apparent activation energy of diffusivity (C) correlate in case of AIST. (A) The ratio of second and first coordination shell radii, r_2/r_1, shows a transition for the two PCMs AIST (red) and $Ge_{15}Sb_{85}$ (blue) in the supercooled regime, both refined by an error function as guide to the eye and to determine the structural transition temperatures T_{LL} (inflexion points) of 660 and 610 K, respectively, visualized by vertical dotted lines. Vertical dashed lines represent the temperature, where ~90% of the low temperature structure are reached and coincide with the FTS crossover temperature. Crosses and circles denote the data points obtained from $\{t_a\}$ and $\{t_b\}$, respectively, while triangles are obtained from the initial structures. A similar transition was reported for $Ge_{15}Te_{85}$ (grey) at the melting point(*24*). **(B)** Simultaneously, a pre-peak is formed, which is related to additional MRO caused by a Peierls distortion. The structural parameters are found to correlate with an increase of the apparent activation energy E_A of inverse diffusivity **(C)**. The latter data are derived from measurements of viscosity above T_m (crosses(*43*)) and from

crystal growth velocities in the supercooled liquid (triangles(*12*)) and glassy regime (circles(*9*) and squares(*58*)), as shown in **(D)**. The solid line corresponds to the model proposed by Orava et al. describing the FTS crossover between two liquids(*20*). Glass transition temperatures (diamonds) are shown for $Ge_{15}Te_{85}$(*59*) and for AIST(*45*), for which literature values show a wide spread.

Fig. 5. AIMD simulations of melt-quenching $Ge_{15}Sb_{85}$ and AIST show the onset of Peierls-distortions upon cooling. (A) We observed R to increase continuously during the quench with initial and final values similar to experimental values, except that the transition is wider in the simulation due to the higher quench rate. **(B, C)** Nearest neighbor histograms of Sb atoms in $Ge_{15}Sb_{85}$ show a continuous six-fold coordination in the high temperature liquid state, whereas they split into three short and three more widely spaced distances in the quenched phase. **(D)** We observed the opening of a pseudogap during the quench in $Ge_{15}Sb_{85}$, but also in AIST (data not shown). **(E, F)** ALTBC plots provide evidence for the formation of a Peierls-distortion by including only the interatomic distances on opposite sides of Sb atoms.

References and Notes:

1. M. Hilbert, P. López, The World ’s Technological Capacity. *Science*. **332**, 60–66 (2011).
2. S. Raoux *et al.*, in *2007 Non-Volatile Memory Technology Symposium* (IEEE, 2007; http://ieeexplore.ieee.org/document/4389940/), vol. 5, pp. 30–35.
3. H. P. Wong *et al.*, Phase Change Memory. *Proc. IEEE*. **98**, 2201–2227 (2010).
4. M. Wuttig, N. Yamada, Phase-change materials for rewriteable data storage. *Nat. Mater.* **6**, 824–832 (2007).
5. F. Xiong, A. D. Liao, D. Estrada, E. Pop, Low-power switching of phase-change materials with carbon nanotube electrodes. *Science*. **332**, 568–570 (2011).
6. F. Rao *et al.*, Reducing the stochasticity of crystal nucleation to enable subnanosecond memory writing. *Science*. **358**, 1423–1427 (2017).
7. D. Loke *et al.*, Breaking the Speed Limits of Phase-Change Memory. *Science*. **336**, 1566–1569 (2012).
8. J. Siegel, C. N. Afonso, J. Solis, Dynamics of ultrafast reversible phase transitions in GeSb films triggered by picosecond laser pulses. *Appl. Phys. Lett.* **75**, 3102–3104 (1999).
9. M. Salinga *et al.*, Measurement of crystal growth velocity in a melt-quenched phase-change material. *Nat. Commun.* **4**, 2371 (2013).
10. R. Jeyasingh *et al.*, Ultrafast characterization of phase-change material crystallization properties in the melt-quenched amorphous phase. *Nano Lett.* **14**, 3419–26 (2014).
11. J. Orava, A. L. Greer, B. Gholipour, D. W. Hewak, C. E. Smith, Characterization of supercooled liquid Ge2Sb2Te5 and its crystallization by ultrafast-heating calorimetry. *Nat. Mater.* **11**, 279–283 (2012).
12. P. Zalden, A. von Hoegen, P. Landreman, M. Wuttig, A. M. Lindenberg, How supercooled liquid phase-change materials crystallize: Snapshots after femtosecond optical excitation. *Chem. Mater.* **27**, 5641 (2015).
13. W. Zhang *et al.*, How fragility makes phase-change data storage robust: insights from ab

initio simulations. *Sci. Rep.* **4**, 6529 (2014).

14. D. Turnbull, Under what conditions can a glass be formed? *Contemp. Phys.* **10**, 473–488 (1969).
15. C. A. Angell, Formation of glasses from liquids and biopolymers. *Science*. **267**, 1924–1935 (1995).
16. V. V Vasisht, S. Saw, S. Sastry, Liquid-liquid critical point in supercooled silicon. *Nat. Phys.* **7**, 549–553 (2011).
17. I. Saika-Voivod, P. H. Poole, F. Sciortino, Fragile-to-strong transition and polyamorphism in the energy landscape of liquid silica. *Nature*. **412**, 514–517 (2001).
18. S. Wei, P. Lucas, C. Austen Angell, C. A. Angell, Phase change alloy viscosities down to T g using Adam-Gibbs-equation fittings to excess entropy data: A fragile-to-strong transition. *J. Appl. Phys.* **118**, 034903 (2015).
19. C. A. Angell, Water II is a "Strong" Liquid. *J. Phys. Chem.* **97**, 6339–6341 (1993).
20. J. Orava, D. W. Hewak, A. L. Greer, Fragile-to-Strong Crossover in Supercooled Liquid Ag-In-Sb-Te Studied by Ultrafast Calorimetry. *Adv. Funct. Mater.* **25**, 4851 (2015).
21. S. Wei, G. J. Coleman, P. Lucas, C. A. Angell, Glass Transitions, Semiconductor-Metal Transitions, and Fragilities in Ge − V − Te (V = As , Sb) Liquid Alloys: The Difference One Element Can Make. *Phys. Rev. Appl.* **7**, 034035 (2017).
22. J. Errington, P. Debenedetti, Relationship between structural order and the anomalies of liquid water. *Nature*. **409**, 318–321 (2001).
23. S. Hechler *et al.*, Microscopic evidence of the connection between liquid-liquid transition and dynamical crossover in an ultraviscous metallic glass former. *Phys. Rev. Mater.* **2**, 1–6 (2018).
24. S. Wei *et al.*, Structural evolution on medium-range-order during the fragile-strong transition in Ge15Te85. *Acta Mater.* **129**, 259–267 (2017).
25. P. G. Debenedetti, H. E. Stanley, Supercooled and Glassy Water. *Phys. Today*. **56**, 40 (2003).
26. D. T. Limmer, D. Chandler, The putative liquid-liquid transition is a liquid-solid transition in atomistic models of water. II. *J. Chem. Phys.* **138** (2013), doi:10.1063/1.4807479.
27. K. H. Kim *et al.*, Maxima in the thermodynamic response and correlation functions of deeply supercooled water. *Science*. **358**, 1589–1593 (2017).
28. P. H. Poole, F. Sciortino, U. Essmann, H. E. Stanley, Phase behaviour of metastable water. *Nature*. **360**, 324–328 (1992).
29. J. C. Palmer *et al.*, Metastable liquid-liquid transition in a molecular model of water. *Nature*. **510**, 385–388 (2014).
30. K. Binder, Simulations clarify when supercooled water freezes into glassy structures. *Proc. Natl. Acad. Sci.* **111**, 9374–9375 (2014).
31. S. Wei, Z. Evenson, M. Stolpe, P. Lucas, C. A. Angell, Breakdown of the Stokes-Einstein Relation Above the Melting Temperature in a Liquid Phase-Change Material. *Sci. Adv.* **4**,

eaat8632 (2018).

32. G. Eising, T. Van Damme, B. J. Kooi, Unraveling crystal growth in GeSb phase-change films in between the glass-transition and melting temperatures. *Cryst. Growth Des.* **14**, 3392–3397 (2014).

33. Y. Chen, C. Rettner, Y. C. Chen, S. Raoux, G. Burr, Ultra-thin phase-change bridge memory device using GeSb. *2006 Int. Electron Devices Meet.*, 1–4 (2006).

34. R. Alonso-Mori *et al.*, Photon-in photon-out hard X-ray spectroscopy at the Linac Coherent Light Source. *J. Synchrotron Radiat.* **22**, 612–620 (2015).

35. M. J. Shu *et al.*, Ultrafast terahertz-induced response of GeSbTe phase-change materials. *Appl. Phys. Lett.* **104**, 251907 (2014).

36. L. Waldecker *et al.*, Time-domain separation of optical properties from structural transitions in resonantly bonded materials. *Nat. Mater.* **14**, 991–995 (2015).

37. P. Zalden *et al.*, Supplementary Materials to "Femtosecond X-ray diffraction reveals a liquid-liquid phase transition in phase-change materials." *Science* (2019).

38. W. K. Njoroge, M. Wuttig, Crystallization kinetics of sputter-deposited amorphous AgInSbTe films. *J. Appl. Phys.* **90**, 3816–3821 (2001).

39. J. Kalb, F. Spaepen, M. Wuttig, Calorimetric measurements of phase transformations in thin films of amorphous Te alloys used for optical data storage. *J. Appl. Phys.* **93**, 2389 (2003).

40. P.-Y. Chewvalier, A thermodynamic evaluation of the Ge-In, Ge-Pb, Ge-Sb, Ge-Tl and Ge-Zn systems. *Thermochim. Acta*. **155**, 227–240 (1989).

41. A. Chiba *et al.*, Relationship between Peierls distortion and medium-range order in Liquid Group-V elements and liquid Group-IV-VI compounds. *J. Phys. Conf. Ser.* **215**, 012077 (2010).

42. J. Orava, H. Weber, I. Kaban, A. L. Greer, Viscosity of liquid Ag–In–Sb–Te: Evidence of a fragile-to-strong crossover. *J. Chem. Phys.* **144**, 194503 (2016).

43. H. Neumann, W. Matz, W. Hoyer, M. Wobst, Investigation of the structure of molten Ge15Te85 in dependence on temperature. *Phys. status solidi (a …*. **90**, 489–498 (1985).

44. E. Barthélémy, S. Albert, C. Vigreux, A. Pradel, Effect of composition on the properties of Te–Ge thick films deposited by co-thermal evaporation. *J. Non. Cryst. Solids*. **356**, 2175–2180 (2010).

45. J. A. Kalb, M. Wuttig, F. Spaepen, Calorimetric measurements of structural relaxation and glass transition temperatures in sputtered films of amorphous Te alloys used for phase change recording. *J. Mater. Res.* **22**, 748–754 (2007).

46. C. Steimer *et al.*, Characteristic ordering in liquid phase-change materials. *Adv. Mater.* **20**, 4535–4540 (2008).

47. T. Matsunaga *et al.*, From local structure to nanosecond recrystallization dynamics in AgInSbTe phase-change materials. *Nat. Mater.* **10**, 129 (2011).

48. J. Y. Raty *et al.*, Aging mechanisms in amorphous phase-change materials. *Nat. Commun.*

6, 7467 (2015).

49. S. Caravati, M. Bernasconi, T. D. Kühne, M. Krack, M. Parrinello, Coexistence of tetrahedral- and octahedral-like sites in amorphous phase change materials. *Appl. Phys. Lett.* **91**, 171906 (2007).

50. N. F. Mott, R. S. Allgaier, Localized states in disordered systems. *Phys. Status Solidi*. **21**, 343 (1967).

51. Y. Tsuchiya, H. Saitoh, Semiconductor-Metal Transition Induced by the Structural Transition in Liquid Ge15Te85. *J. Phys. Soc. Japan*. **62**, 1272–1278 (1993).

52. S. Hosokawa, Y. Sakaguchi, K. Tamura, X-ray diffraction measurements for liquid As2Se3 up to the semiconductor-metal transition region. *J. Non. Cryst. Solids*. **150**, 35–39 (1992).

53. Y. S. Tver'yanovich, V. M. Ushakov, A. Tverjanovich, Heat of structural transformation at the semiconductor-metal transition in As2Te3 liquid. *J. Non. Cryst. Solids*. **197**, 235–237 (1996).

54. M. Schumacher *et al.*, Structural, electronic and kinetic properties of the phase-change material Ge2Sb2Te5 in the liquid state. *Sci. Rep.* **6**, 27434 (2016).

55. M. Wuttig, V. L. Deringer, X. Gonze, C. Bichara, J.-Y. Raty, Incipient Metals: Functional Materials with a Unique Bonding Mechanism. *Adv. Mater.*, 1803777 (2018).

56. J. Y. Raty *et al.*, A Quantum-Mechanical Map for Bonding and Properties in Solids. *Adv. Mater.* **31**, 1–6 (2019).

57. J. P. Gaspard, Structure of covalently bonded materials: From the Peierls distortion to Phase-Change Materials. *Comptes Rendus Phys.* **17**, 389–405 (2016).

58. J. Kalb, F. Spaepen, M. Wuttig, Atomic force microscopy measurements of crystal nucleation and growth rates in thin films of amorphous Te alloys. *Appl. Phys. Lett.* **84**, 5240 (2004).

59. Y. Tsuchiya, Thermodynamics of the structural changes in the liquid Ge–Te system around the Te-rich eutectic composition. *J. Non. Cryst. Solids*. **312**–**314**, 212–216 (2002).

60. H. E. Fischer *et al.*, D4c: A very high precision diffractometer for disordered materials. *Appl. Phys. A Mater. Sci. Process.* **74**, s160–s162 (2002).

61. H. E. Fischer, A. C. Barnes, P. S. Salmon, Neutron and x-ray diffraction studies of liquids and glasses. *Reports Prog. Phys.* **69**, 233–299 (2006).

62. A. Chiba *et al.*, Pressure-induced suppression of the Peierls distortion of liquid As and GeX (X=S, Se, Te). *Phys. Rev. B*. **80**, 060201 (2009).

63. K. Shportko *et al.*, Resonant bonding in crystalline phase-change materials. *Nat. Mater.* **7**, 653–658 (2008).

64. H. R. Philipp, Optical Properties of Silicon Nitride. *J. Electrochem. Soc.* **120**, 295 (1973).

65. M. J. Shu, I. Chatzakis, Y. Kuo, P. Zalden, A. M. Lindenberg, Ultrafast sub-threshold photo-induced response in crystalline and amorphous GeSbTe thin films. *Appl. Phys. Lett.* **102**, 1903 (2013).

66. J. P. Reifenberg *et al.*, Thermal Boundary Resistance Measurements for Phase-Change Memory Devices. *IEEE Electron Device Lett.* **31**, 56–58 (2010).

67. B. L. Zink, F. Hellman, Specific heat and thermal conductivity of low-stress amorphous Si–N membranes. *Solid State Commun.* **129**, 199–204 (2004).

68. A. Jain, K. E. Goodson, Measurement of the Thermal Conductivity and Heat Capacity of Freestanding Shape Memory Thin Films Using the 3ω Method. *J. Heat Transfer*. **130**, 102402 (2008).

69. P. J. Bendeich, J. M. Barry, W. Payten, Determination of specific heat with a simple inverse approach. *Appl. Math. Model.* **27**, 337–344 (2003).

70. H. Ftouni *et al.*, Specific heat measurement of thin suspended SiN membrane from 8 K to 300 K using the 3ω-Völklein method. *Rev. Sci. Instrum.* **84**, 094902 (2013).

71. P. Zalden *et al.*, Simultaneous calorimetric and quick-EXAFS measurements to study the crystallization process in phase-change materials. *J. Synchrotron Radiat.* **19**, 806–813 (2012).

72. T. P. L. Pedersen *et al.*, Mechanical stresses upon crystallization in phase change materials. *Appl. Phys. Lett.* **79**, 3597–3599 (2001).

73. Johannes Andreas Kalb, thesis, RWTH Aachen University (2006).

74. P. Zalden *et al.*, Atomic structure of amorphous and crystallized Ge15Sb85. *J. Appl. Phys.* **107**, 4312–4319 (2010).

75. W. P. Risk, C. T. Rettner, S. Raoux, Thermal conductivities and phase transition temperatures of various phase-change materials measured by the 3ω method. *Appl. Phys. Lett.* **94**, 1906 (2009).

76. T. E. Faber, J. M. Ziman, A theory of the electrical properties of liquid metals. *Philos. Mag.* **11**, 153–173 (1965).

77. T. E. Faber, *An introduction to the theory of liquid metals* (Cambridge University Press, Cambridge, UK, 1972).

78. P. J. Brown *et al.*, in *International Tables for Crystallography* (2006), vol. C, pp. 554–595.

79. B. L. Henke, E. M. Gullikson, J. C. Davi, X-ray interactions: photoabsorption, scattering, transmission, and reflection at E=50-30000 eV, Z=1-92. *At. Data Nucl. Data Tables*. **54**, 181 (1974).

80. H. Weber *et al.*, Experimental and ab initio molecular dynamics study of the structure and physical properties of liquid GeTe. *Phys. Rev. B*. **96**, 054204 (2017).

Acknowledgments: P.Z. would like to thank Dr. Christophe Bichara for valuable suggestions and discussions. Portions of this research were carried out at the Linac Coherent Light Source (LCLS) at the SLAC National Accelerator Laboratory. LCLS is an Office of Science User Facility operated for the US Department of Energy (DOE) Office of Science by Stanford University. **Funding:** F.Q., A.K., M.N., and K.S.T. gratefully acknowledge financial support by the German Research Council through the Collaborative Research Center SFB 1242 (project

278162697) “Non-Equilibrium Dynamics of Condensed Matter in the Time Domain” (project C01 “Structural Dynamics in Impulsively Excited Nanostructures”), and individual grant So408/9-1, as well as the European Union (7th Framework Programme, Grant No. 280555 GO FAST). M.S., R.M., and M.W. acknowledge financial support by the German Research Council through the Collaborative Research Center SFB 917 ”Nanoswitches” and the individual grant Ma-5339/2-1. M.S., I.R. and R.M. also acknowledge the computational resources granted by JARA-HPC from RWTH Aachen University under Project No. JARA0150 and No. JARA0183. M.T., A.M.L. and D.A.R. were supported by the U.S. Department of Energy, Office of Science, Office of Basic Energy Sciences through the Division of Materials Sciences and Engineering under Contract No. DE-AC02-76SF00515. This work was performed under the auspices of the U.S. Department of Energy by Lawrence Livermore National Laboratory under Contract DE-AC52-07NA27344. J. L. acknowledges the support of the Swedish Science Council (VR).
Author contributions: K.S.T. initiated the project. F.Q. K.S.T. and P.Z. conceived the experiment. P.Z. and M.W. were responsible for sample preparation. F.Q., P.Z., A.K., M.N., J.S., M.T., P.A., H.E., M.S., T.P., J.L., A.M.L., S.H.R., D.A.R., and K.S.T. carried out the experiment. M. S., I.R. and R. M. conceived, performed and evaluated the AIMD simulations. M.C., H.L., and D.Z. operated the X-ray pump-probe instrument. P.Z. analyzed the data with important input from K.S.T., F.Q., A.K., M.N., P.A., H.E., and J.S.. H.E.F. and P.Z. conducted and evaluated the neutron total scattering measurements. P. Z. and K.S.T. wrote the manuscript with specific contributions from A.M.L., M.W. and S.W. and comments from all other authors; **Competing interests:** Authors declare no competing interests; **Data and materials availability:** All data and code is available upon request from the corresponding authors.

Supplementary Materials:

Methods and Materials

Figures S1-S27

Tables S1-S3

Methods and Materials

Optical pump, X-ray probe experiments were performed at the X-ray Pump Probe (XPP) instrument of the Linac Coherent Light Source (LCLS) of the Stanford Linear Accelerator Center (SLAC). The experimental setup is depicted schematically in Fig. S1. Frames of Si_3N_4 membranes with thickness of 50 nm (AIST) and 150 nm ($Ge_{15}Sb_{85}$) were coated with 50 and 60 nm thick films of the respective phase-change materials (PCMs) by means of sputter deposition from stoichiometric targets. After each interaction with an optical or X-ray pulse, the sample was translated such that a fresh square membrane, each with 300 µm size was centered on the interaction point of both beams. The optical excitation was conducted using 50 fs duration laser pulses from a Ti:Sapphire chirped pulse amplifier with 800 nm wavelength. The thin film sample was pumped at a small angle less than 10° against normal incidence. The pump spot size was about 150 µm full width at half maximum (FWHM) intensity in diameter 1/e as determined by the imprinting technique. The X-ray probe beam with center wavelength of 1.305 Å was incident normal to the sample film and was focused by beryllium lenses to a spot size of 30 µm FWHM. Both beams interacted with the sample which was held at an ambient temperature of about 298 K

in vacuum. A MarCCD 2D area detector was used to record the X-ray diffraction pattern from each X-ray probe pulse individually.

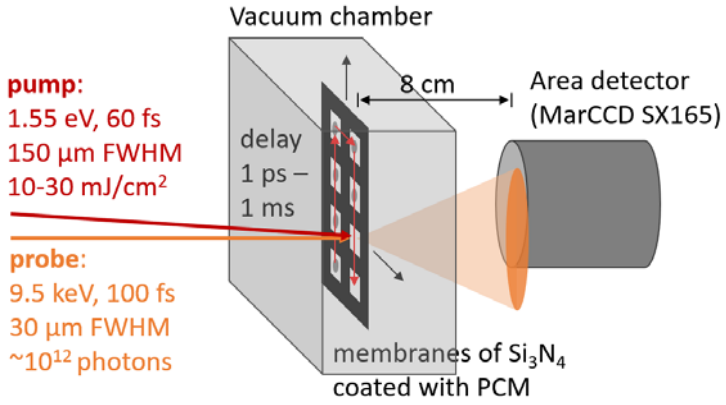

Fig. S1. The experimental setup at the XPP instrument of LCLS is shown schematically.

To demonstrate the impact of the short available q-range, limited by the photon energies available at free electron lasers (FELs) so far, we compare in Fig. S2 the diffraction data of as-deposited AIST obtained in the present experiment (green curve) with those obtained by neutron total scattering at the D4 instrument of the Institut Laue-Langevin (ILL), see the purple curve in Fig. S2. Details on the neutron total scattering experiment are available in section II of the SI. Up to 4 $Å^{-1}$, the diffraction data obtained with both techniques are very similar - as expected considering the similar ratio of neutron and X-ray cross sections of Sb and Te. Since the neutron diffraction data reveal oscillations in the structure factor extending up to almost 20 $Å^{-1}$, we can demonstrate the impact of the limited q-range at ambient conditions in Fig. S2b. At elevated temperatures, the Debye Waller factor acts dominantly on the high-q part of the structure factor and thereby further reduces the importance of the higher q-range missing in the X-ray data. The pair correlation function obtained by neutron total scattering resolves additional features within the second coordination shell (see Fig. S2b), but most importantly the center of mass of the first and second coordination shells can be extracted from the X-ray data despite the limited q-range. From the neutron total scattering data, one obtains for the as-deposited amorphous state of AIST R=1.51±0.01 with the first distance at r_1=2.84 Å and the second at r_2=4.28 Å. This number is in good agreement with the value obtained from the X-ray data for the initial state, R=1.51±0.01 for AIST, as well as $Ge_{15}Sb_{85}$ (R=1.52±0.01, data not shown here).

Using the D4 neutron diffractometer(*60*) at the Institut Laue-Langevin (ILL) in Grenoble (France), all neutron total scattering experiments were performed on as-deposited amorphous samples, obtained by scratching films of about 500 nm thickness from silica glass slides. The powder is then filled into quartz capillaries of 10 µm wall thickness and an outer diameter of 1.9 mm. The sealed capillaries are filled such that the neutron interact with a homogeneously filled slab of the capillary. Scattering measurements are performed with monochromatized neutrons at 0.4976 A. Background measurements are performed with an empty capillary and with an empty instrument. The procedure to remove the background signals and to calibrate the raw experimental data is described elsewhere(*61*). Subsequently, we employ the Placzek

correction to remove the inelastic scattering contribution and subtract the self-scattering term(*61*). Further dividing by $\langle b \rangle^2$, we obtain $S(q) - 1$, with $S(q)$ plotted in Fig. 2 of the main manuscript.

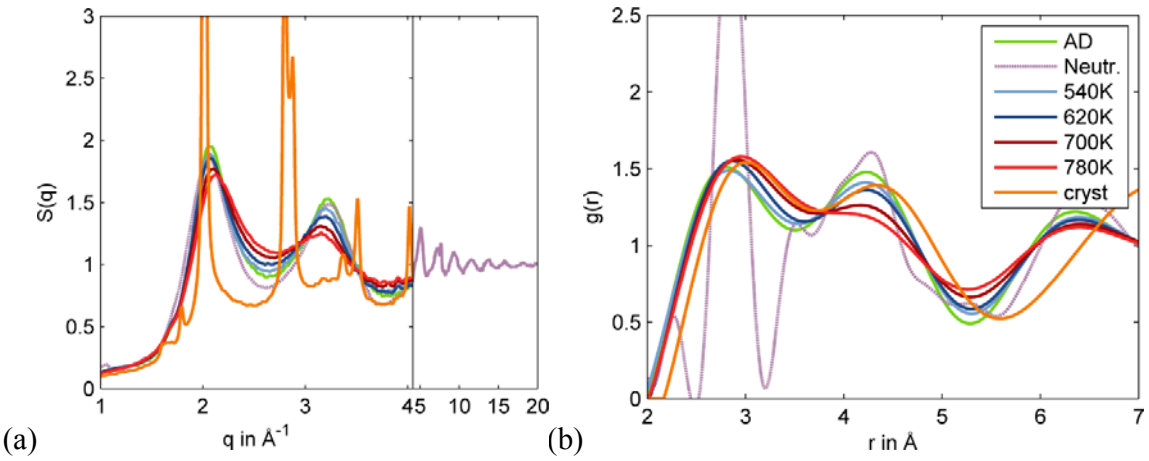

Fig. S2 *shows the impact of the limited q-range in the x-ray laser diffraction (green curve) by comparison with neutron total scattering data extending out to 20 Å^{-1} (purple curve). Additional features in the pair correlation function g(r) are resolved in the neutron data, but the ratio of real space coordination shells deviates by less than 1%.*

Direct evidence for the onset of a Peierls-distortion: Pre-peak in S(q)

During the quench of AIST and $Ge_{15}Sb_{85}$, a pre-peak becomes visible in the S(q) experimental data in Fig. S3 at a momentum transfer of 1.08±0.02 and 1.06±0.02 Å^{-1}, respectively. They correspond to periodic structures in real space with 5.8 and 5.9 Å, respectively and match very accurately twice the distance of the first coordination shell r_1. This doubling of the atomic periodicity implies that two opposite bonds form an alternating sequence of short and long distances, as also revealed by the AIMD simulations and visualized by the angular-limited bond correlation (ALTBC) plots (see Figs. S10a&b)). Both, experiment and simulation show the presence of this distortion only in the supercooled liquid state - not in the equilibrium liquid. This formation of an atomic distortion is driven by the energy gain due to the opening of a band gap and corresponds to the textbook picture of such a distortion. A similar observation of a pre-peak in S(q) in liquid materials with three p-electrons has been reported by Chiba et al., who have investigated the equilibrium liquid phases of As, GeS, GeSe and GeTe. They equally relate the pre-peak to a Peierls distortion, which they show can be suppressed by applying pressure(*41*, *62*). In the S(q)'s derived from our AIMD simulations, the pre-peak is not directly visible, but interestingly, two pre-peaks indicating an oscillation are formed at q=0.8 and 1.3 Å^{-1} in case of $Ge_{15}Sb_{85}$ and at 0.9 and 1.4 Å^{-1} in case of AIST, see Fig. S6. Their periodicity of 0.5 Å^{-1} originates from relatively sharp features at 12 Å in real space and matches the cut-off of half the simulation cell size used in the calculation of g(r). These oscillations in S(q) are dominating over the small amplitude of the pre-peak observed experimentally.

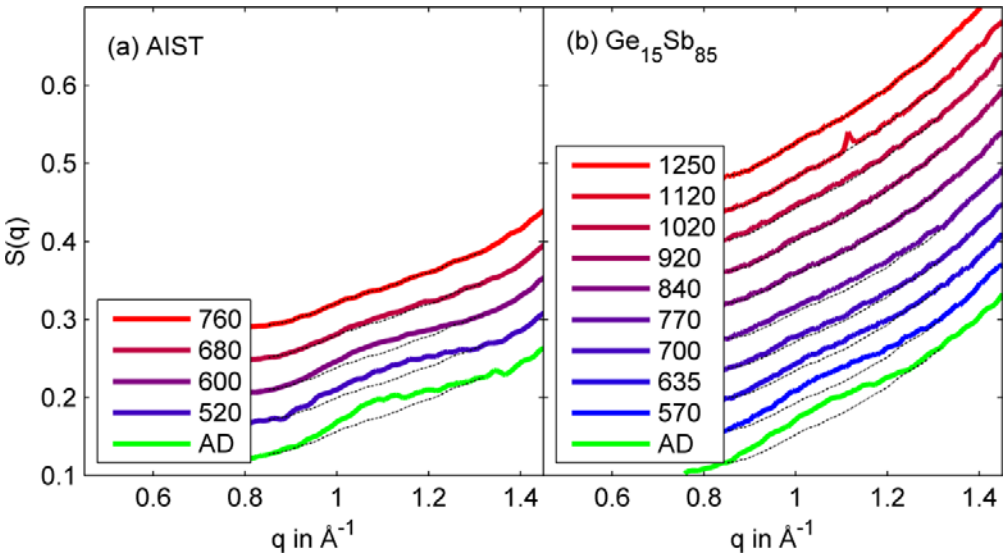

Fig. S3 shows the raw diffraction data around the pre-peak region at various temperatures, given in Kelvin in the legend and for the as-deposited (AD) state at ambient conditions. The dashed black line corresponds to the high T case, where no pre-peak is visible and is used as baseline in the integration of the pre-peak intensity. Curves are stacked with a vertical increment of 0.04.

Cubic AIST in the "final" state

Fig. S4 shows the diffraction pattern obtained for AIST after infinite delays. At lowest fluences, the sample does not crystallize, but remains amorphous. Crystallization of a cubic phase sets in upon exceeding 14.5 mJ/cm^2. At fluences above 23 mJ/cm^2, the regular hexagonal phase of AIST is obtained, whose reflections are included as grey vertical lines(*38*). No further transitions are observed up to 40 mJ/cm^2. Fluctuations in intensity of the different reflections are due to the random orientation of larger crystalline grains. Fluctuations in momentum transfer of the reflections are dominated by the photon energy instability due to the SASE process of the x-ray free electron laser.

If, on the other hand, the laser fluence is not sufficiently high to induce crystallization (less than 14.5 mJ/cm^2), the amorphous state is eventually restored.

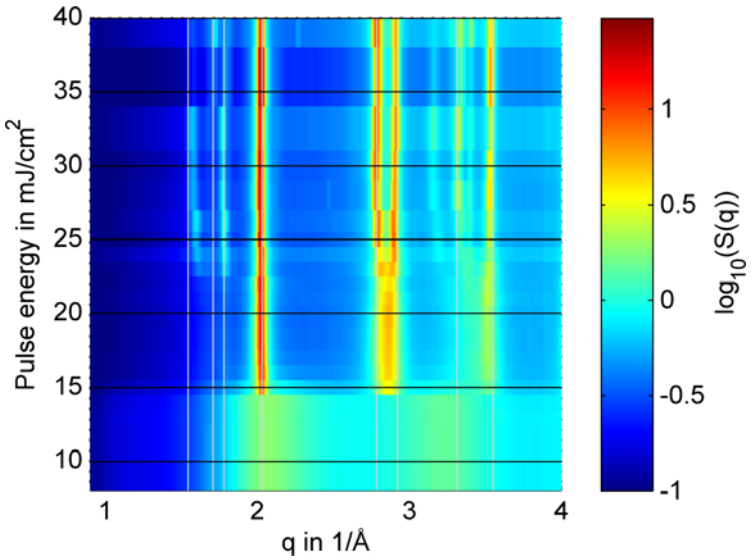

Fig. S4 *shows the structure factors S(q) of AIST obtained for infinite pump probe delays ("final" state). The data reveal the crystallization thresholds of a cubic structure at 14.5 mJ/cm^2 and of the common hexagonal structure at 23 mJ/cm^2.*

Thermal Simulations

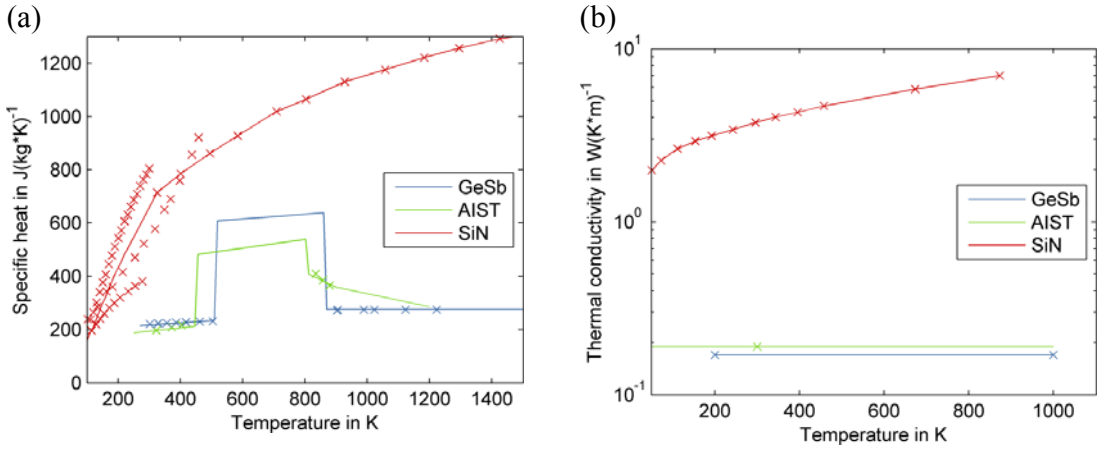

(c)

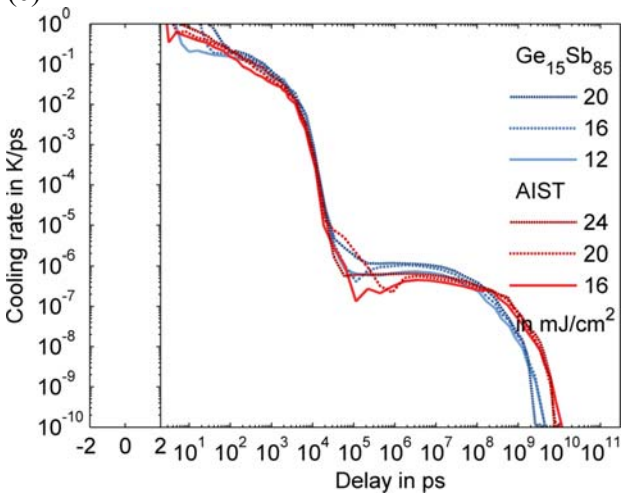

Fig. S5 *shows the thermodynamic properties used for the simulation of heat flow inside the PCMs.*

The absolute temperature for the PCMs following femtosecond optical excitation is calculated based on finite element simulations, modeled with literature values for the thermal and dielectric properties of all materials involved. The initial energy density deposited by the optical pulse is calculated based on the complex dielectric function of the as-deposited amorphous PCMs(*63*) and silicon nitride(*64*). Interference effects of reflected waves are fully considered, considering multiple reflections via the Fresnel equations. We assume that electron-phonon scattering is sufficiently fast, such that diffusion of photoexcited carriers can be neglected. This is justified by the picosecond relaxation times observed in earlier all-optical pump-probe experiments(*65*). Given the deposited heat density as a function of the position through the layer stack, finite element simulations are performed to extract the average temperature of the phase-change film as a function of time, while the heat is transferred into the membrane. These simulations consider the temperature-dependent specific heats and thermal conductivities of all materials involved. An additional thermal boundary resistance of 2E-8 K*m²/W is implemented to describe the interface between the PCM and the nitride layer(*66*). The specific heat data and thermal conductivities are shown in Fig. S5a.The specific heat data on SiN (red crosses)(*67–70*) are averaged to obtain the data represented by the red line, which was used in the simulations. In case of PCMs, only the specific heat of the amorphous and crystalline states is known and in the exceptional case of AIST also for the liquid state. In our experimental case, we need to consider only the specific heat of the disordered state - from the liquid phase to the glass. Since no information on the exact specific heat are available for the supercooled liquid state, we approximate it based on common models. In this specific heat, also the known enthalpy difference between the amorphous and liquid states must be included. This is determined by subtracting the enthalpy of crystallization for the amorphous material from the enthalpy of melting of the crystalline material. Both quantities are known accurately from previous studies and amount to (16.1 - 4.2) kJ/mol = 11.9 kJ/mol for AIST (*39*) and (21.5 - 4.9) kJ/mol = 16.6 kJ/mol for $Ge_{15}Sb_{85}$ (*71–73*). These heats are added to the specific heats linearly interpolated from literature data for AIST(*39*) and $Ge_{15}Sb_{85}$ and equally distributed over the temperature range from the crystallization temperature

(at about 1 K/s heat rate) and the temperature of fusion, 512 and 865 K in case of $Ge_{15}Sb_{85}$ (*74*)(*40*) as well as 441 and 807 K for AIST (*39*). This results in an additional specific heat of 32.5 J/mol/K for AIST and 47.0 J/mol/K for $Ge_{15}Sb_{85}$. It is important to stress that the resulting specific heat is almost constant in the temperature range from 500 to 700 K, where the liquid-liquid phase transition is observed. Given the weak temperature-dependence of the thermal conductivity of AIST and $Ge_{15}Sb_{85}$, at least up to 450 K, we model them with the temperature independent value reported previously(*75*).

Ab Initio Molecular Dynamics Simulations

The computational results presented in this work have been obtained from ab initio models of $Ge_{15}Sb_{85}$ and AIST. The generation of the melt-quenching models is described in the section *Ab initio molecular dynamics* of the main text, here we give further details on the composition, dimension and number density of the ab initio models. The models comprise simulation cells containing several hundred atoms and are chosen large enough to describe the structural evolution of the two compounds upon melt-quenching reasonably well.

Compound**:**	Composition:	Dimensions: [Å³]	Number density: [1/Å³]
$Ge_{15}Sb_{85}$ 360 atoms	Ge: 54 atoms, Sb: 306 atoms	21.765×22.619×22.781	0.0321
AIST 540 atoms	Ag: 20, In: 16, Sb: 360, Te: 144	25.979×25.979×25.979	0.0308

Table S1: *Compositions, cell dimensions and number densities of the ab initio models employed to simulate the different stages of the melt-quenching process of $Ge_{15}Sb_{85}$ and AIST. The model densities correspond to the densities of the amorphous phases of $Ge_{15}Sb_{85}$ and AIST*(*39*)*.*

The number densities correspond to experimental values for the amorphous phase(*39*) and are kept constant throughout the whole melt-quenching process, i.e., effects of thermal expansion/contraction are neglected. Table S1 lists the defining properties of the cells/models.

Analysis of Ab initio Data

Structure factors:

The most direct way to compare the results obtained from AIMD simulations to the experimental scattering results is the comparison of structure factors from both sources, since then the limited q-range of the experimental data does not cause issue upon Fourier transformation and comparing in real space. We describe here the methods and algorithms used to calculate the XRD structure factors based on AIMD trajectory data. In order to obtain XRD structure factors computationally, we first calculate the partial radial distribution functions by means of creating an interparticle distances histogram (averaged over the 2,500 MD steps or 5 ps of a single section of the AIMD trajectory with constant setting temperature) resolved by the species of the particle pairs counted:

$$g_{\alpha\beta}^{k} = g_{\alpha\beta}(r_k) = \frac{V}{N_\alpha(N_\beta - \delta_{\alpha\beta})}\frac{\langle h_{\alpha\beta}(r_k)\rangle}{4\pi r_k^2 \Delta r}$$

The result is a discrete set of values $g_{\alpha\beta}(r_k)$, evaluated at distances $r_k = (k + 1/2)\Delta r, k = 0,1,2, \ldots$, that is, however, treated usually as a continuous function of the radial variable $r_k \rightarrow r$ if the discretization length Δr is sufficiently small. $\delta_{\alpha\beta}$ denotes the Kronecker symbol, evaluated to 1 for identical atomic species $\alpha = \beta$ and equal to 0 otherwise.

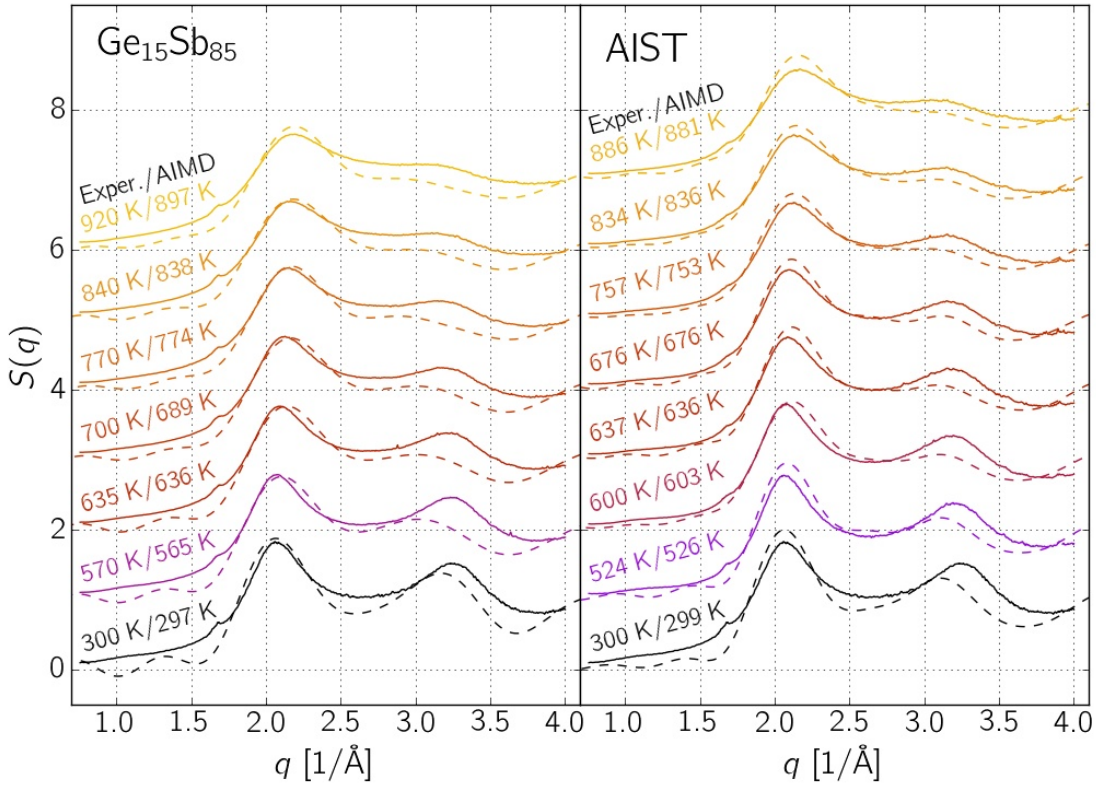

Fig. S6 *gives a direct comparison between computationally and experimentally obtained XRD structure factors at corresponding temperatures for both the melt-quenching process of* $Ge_{15}Sb_{85}$ *and AIST. A qualitative agreement is obvious.*

From the partial radial distributions, we calculate in the next step the partial structure factors by means of a Fourier transform, following the notation by Faber and Ziman (FZ)(*76*, *77*), and get

$$S_{\alpha\beta}^{FZ}(q) = 1 + 4\pi\rho \int dr\, r^2 \frac{\sin(qr)}{qr}\left(g_{\alpha\beta}(r) - 1\right)$$

The total (XRD) structure factor is then obtained summing up the weighted partial contributions according to

$$S(q) = 1 + \sum_{\alpha\beta} c_\alpha f_\alpha c_\beta f_\beta^* \left(S_{\alpha\beta}^{FZ}(q) - 1\right)$$

$$S(q) = \frac{\sum_{\alpha\beta} c_\alpha f_\alpha c_\beta f_\beta^* S_{\alpha\beta}^{FZ}(q)}{\sum_{\alpha\beta} c_\alpha f_\alpha c_\beta f_\beta^*}$$

where $c_\alpha = N_\alpha/N$ gives the fraction of atoms of species α in terms of the total number of atoms and f_α is the atomic form factor of species α. The latter quantity is estimated via

$$f_\alpha = f_\alpha^0 + f_\alpha^{Henke} - Z_\alpha$$

where f_α^0 is the q-dependent scattering factor(*78*) obtained from integration of the electronic charge density, $f_\alpha^{Henke} = f_\alpha^1 + i\, f_\alpha^2$ is calculated from tabulated, energy dependent values(*79*) and Z_α is the atomic number of species α. Applying the described scheme to both $Ge_{15}Sb_{85}$ and AIST data for sections of the AIMD trajectory with average temperatures as close as possible to the temperatures of the scattering experiments and plotting the corresponding structure factors from both sources together results in the curves displayed in Fig. S6. We observe a qualitative agreement between scattering experiments and computational results for both compounds at all temperatures considered, supporting the assumption that the AIMD simulations provide valid models of the atomic structure of $Ge_{15}Sb_{85}$ and AIST and its evolution during melt-quenching.

For a reasonable analysis of the local coordination, bonds, bond motifs and bond angles, it is necessary to choose the radial cutoffs consistently first. Throughout the entire analysis of AIMD trajectory data in this study, the cutoff values given in Table S2 are used to distinguish bonds from unbonded atom pairs. The cutoffs are chosen as the positions of the first minima of the respective partial radial distribution functions for all cases where this value does not exceed the position of the first minimum of the total radial distribution function. Otherwise, the position of the first minimum of the total radial distribution function is used as the cutoff for the respective species pair. In case this total cutoff turns out to be larger than 3.40 Å, the latter value is used as a threshold to all the partial radial cutoffs. This situation holds for all partial cutoffs applied in the analysis of the melt-quenching of AIST, as the table shows.

Compound	Species pairs and cutoffs in Å (first minima positions in Å)									
$Ge_{15}Sb_{85}$ total: 3.275	Ge-Ge:			Ge-Sb:			Sb-Sb:			
	3.025			3.225			3.275			
AIST total: 3.40 (3.595)	Ag-Ag	Ag-In	Ag-Sb	Ag-Te	In-In	In-Sb	In-Te	Sb-Sb	Sb-Te	Te-Te
	3.40 (3.785)	3.40 (4.055)	3.40 (3.525)	3.40 (3.605)	3.40 (4.785)	3.40 (3.545)	3.40 (3.765)	3.40 (3.595)	3.40 (3.775)	3.40 (5.445)

Table S2: *Radial cutoffs applied in the analysis of various structural properties. The positions of the first minima extracted from the partial radial distributions are printed in brackets where they differ from the applied cutoffs.*

Pair correlation functions:

The atomic partial pair correlation functions, shown in Figs. S7&8 for the cases of $Ge_{15}Sb_{85}$ and AIST, respectively, confirm that the first coordination shell around the majority element (Sb) decreases significantly during the quench. The Sb-Sb correlation in $Ge_{15}Sb_{85}$, shown in Fig. S7 confirms in particular that r_1 shifts from 3.05 Å in the liquid state at 834 K to 2.94 Å at ambient conditions, consistent with the experimental observation.

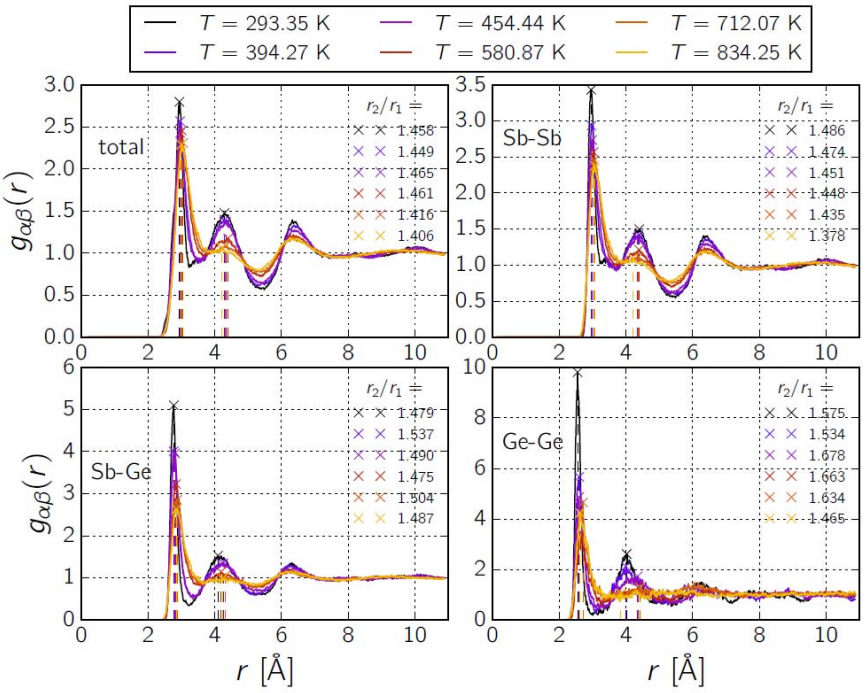

Fig. S7. Total and partial pair correlation functions of $Ge_{15}Sb_{85}$, showing the decrease of r_1 during the quench as well as the pronounced changed of amplitude in g(r) around r_2.

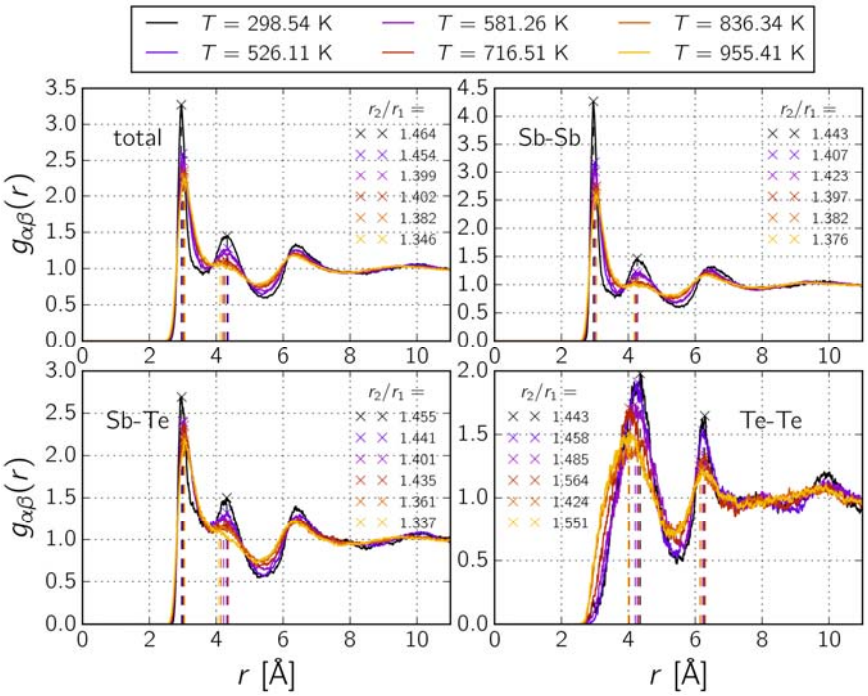

Fig. S8. Total and partial pair correlation functions of AIST, showing the decrease of r_1 during the quench as well as the pronounced changed of amplitude in g(r) around r_2.

Bond number statistics:

The most basic structural property directly obtainable from AIMD trajectory data, which still gives a good insight into bonding properties, are the partial bond numbers. The analysis is a simple counting of atom pairs, approving their distance fulfills the cutoffs specified in Table S2 and accounting for them depending on the species of the atom pairs sampled. Averages over a number of 2,500 MD steps (or 5 ps, respectively) give the ratio of partial to total bond number, as plotted in Figs. S6a, b&c as function of the effective simulation temperature along the AIMD melt-quenching trajectory. The partial bond numbers for minority-minority species pairs, i.e. Ag-Ag, Ag-In and In-In, are not depicted because of their negligibly small contribution to the total number of bonds and the correspondingly bad statistics of these partials. For the melt-quenching of $Ge_{15}Sb_{85}$, we obtain increasing numbers of homopolar Sb-Sb and Ge-Ge bonds, whereas the number of Sb-Ge bonds decreases with decreasing temperature. The partial bond numbers stay almost constant above 600 K, though fluctuating strongly, especially in the case of Ge-Ge bonds. The fluctuations of bond numbers in the upper half of the melt-quenching temperature interval are the strongest for Ge-Ge bonds, with approximately 10%. They are smaller for Sb-Ge bonds, accounting for about 2%, and Sb-Sb bonds with about 1%. In contrast to the comparably strong fluctuations in this part of the temperature range, in the lower half of the temperature range, starting at about T = 600 K, the bond number curves start showing the defined trends ascribed above and the fluctuations get weaker. The thereby occurring kink is located close to the temperature of the structural transition observed in our experimental results, T = 610 K, for all three curves. Dominant are the Sb-Sb and Sb-Ge bonds, amounting to at least 2/3 of the total number of bonds throughout the melt-quenching process.

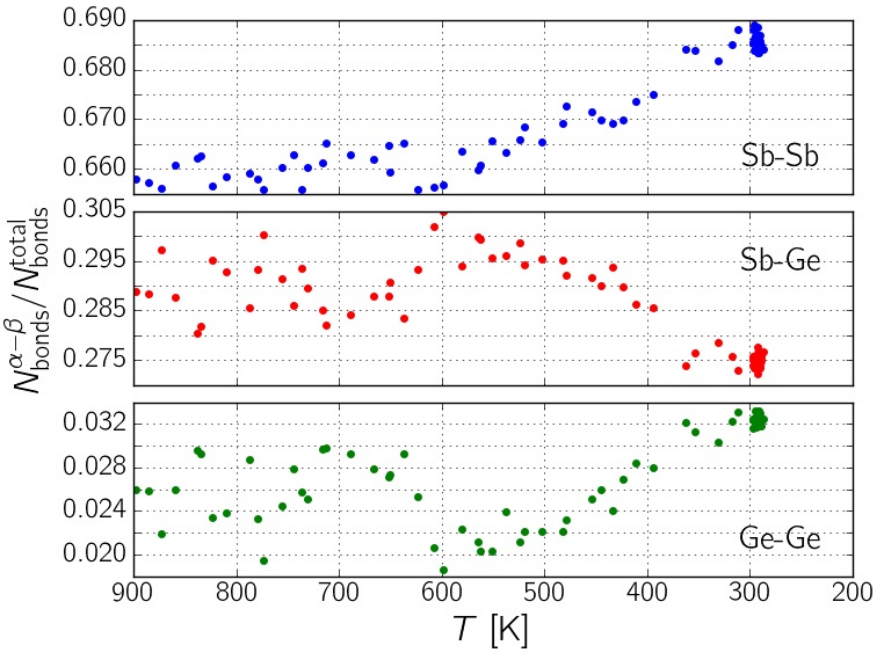

Fig. S9. *Temperature evolution of partial bond numbers upon melt-quenching of $Ge_{15}Sb_{85}$ in terms of the total number of bonds.*

In the case of melt-quenching AIST, trend-changes of the bond-number-curves were observed in a similar temperature range. Contrary to the situation discussed for $Ge_{15}Sb_{85}$, the majority-majority species bond number partials are almost constant in the lower part of the investigated temperature range, between 300 K and 600 K. The increases, found for Sb-Sb and Sb-Te bond numbers in the upper part, between 600 K and 1000 K, are small (about 1% each), as the reduction of Te-Te bond numbers is within 2% of the total number of bonds. However, the number of Te-Te bonds drops by 2/3 in relative terms. The fluctuations of bond numbers are again strong compared to the increases observed for Sb-Sb and Sb-Te bonds. The fluctuations are comparably small for Te-Te bonds, though. Trend changes are also visible for the minority-majority species bond number partials although it needs to be mentioned that these values are prone to weak statistics because of the low amount of Ag and In atoms in the model (see Table S1 for compositional details). The kink in the Ag-Sb and Ag-Te curves is therefore not necessarily a feature of the melt-quenching process. Further investigations are needed to verify this observation but are beyond the scope of this work. However, it is worth mentioning that this double-kink occurs again closely to the temperature identified as the point where the structural transition is concluded to happen in the experiment. The most obvious trend visible in the minority-majority curves is the tendency of both Ag and In atoms to release bonds to Sb atoms in favor of the formation of bonds with Te. Keeping in mind that the minority-majority bonds contribute with approximately 15% to the total number of bonds these effects are not negligible.

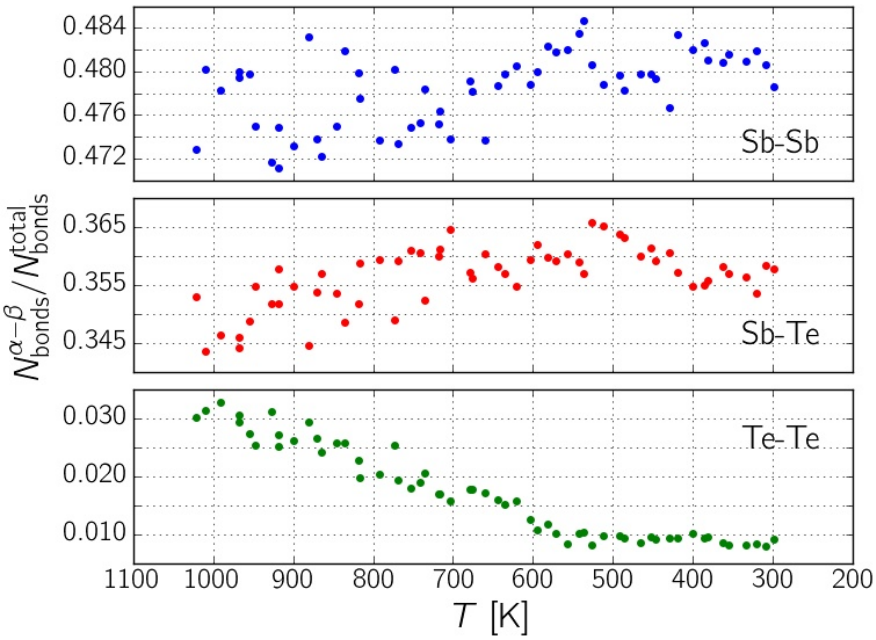

Fig. S10. *Temperature evolution of partial majority-majority bond numbers upon melt-quenching of AIST in terms of the total number of bonds.*

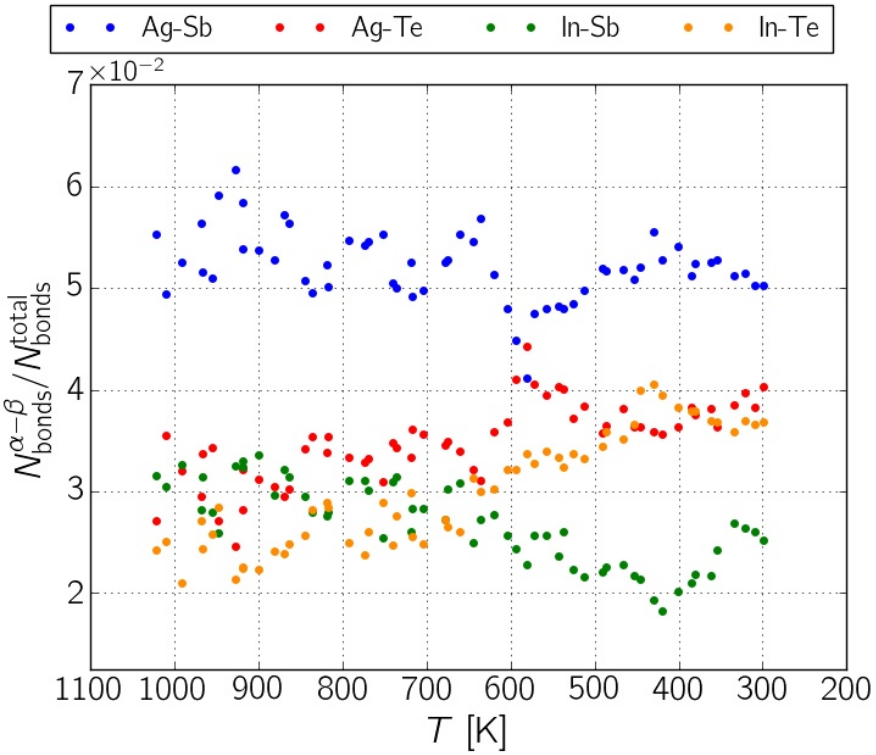

Fig. S11. *Temperature evolution of partial minority-majority bond numbers upon melt-quenching of AIST in terms of the total number of bonds.*

Bond order parameter statistics:

In addition to simple bond numbers, we analyze the bond order configuration evolution upon melt-quenching following the AIMD trajectory from the liquid to the amorphous phase, in the course of which we categorize atoms by the local structural motif they are contained in. These structural motifs are identified through evaluation of the bond order parameter(*22*)

$$q = q_k = 1 - \frac{3}{8}\sum_{i=1}^{N_k^{nb}}\sum_{j=i+1}^{N_k^{nb}}\left(\frac{1}{3} + \cos(\Theta_{ikj})\right)^2,$$

counted according to the categories(*80*) summarized in Table S3 and the numbers obtained averaged over MD step sets with constant setting temperature. Here, Θ_{ikj} is the angle between distance vectors connecting an atom k to its nearest neighbors i and j. The summation runs over all pairs (i,j) of atoms $i,j = 1, \cdots, N_k^{nb}$ bound to an atom k. Again, the cutoffs from Table S2 are applied to separate bonds from simple atom pairs with a larger inter-particle distance and we average over 5 ps for every single data point of the temperature evolution obtained.

Motif:	3-fold defective octahedral	4-fold defective octahedral	5-fold defective octahedral	6-fold octahedral	4-fold tetrahedral	others
q-Parameter:	0.8 < q < 1.0 (≈7/8)	0.5 < q < 0.8 (≈5/8)	0.1 < q < 0.5 (≈1/3)	-0.1 < q < 0.1 (≈0)	0.8 < q < 1.0 (≈1)	other q values

Table S3: *The different local bond motifs and associated ranges of the q parameter. Motif characteristic q-values(80) are given in brackets below the corresponding q-intervals.*

The results of this procedure, applied to the $Ge_{15}Sb_{85}$ AIMD trajectory, are displayed in Fig. S12. Sb atoms in this compound tend to enhance coordination in 3- and 4-fold defective octahedral motifs as temperature decreases, the share of 5-fold defective octahedral structures does not obey any clear trend and 6-fold octahedra are rare. As Sb does not have any preference for tetrahedral coordination, the number of Sb-centered tetrahedra is small as well. On the contrary, the fraction of Ge tetrahedra increases up to 70% of all Ge atoms during melt-quenching, starting from a low level of about 10% at high temperature. The number of atoms in defective octahedral coordination becomes less. The fraction of 6-fold octahedra increases but the absolute number stays small throughout the melt-quenching. The number of both Sb and Ge atoms collected under the tag 'others' gets massively reduced as the order of the system enhances and increasingly many atoms fall under the ordered (defective) octahedral and tetrahedral coordination categories. Again, we obtain signatures of a structural transition at around 600 K. For Sb, the slope of the of 3-fold defective octahedral curve increases, an inflection point of the 4-fold defective octahedra curve occurs, and the 5-fold defective octahedra curve shows a maximum around this temperature. Regarding the Ge-centered configurations, the inclination of the tetrahedra fraction curve increases, the 4-fold defective octahedra curve starts dropping, and the evolution of the 5-fold defective octahedra reveals a maximum in this temperature region.

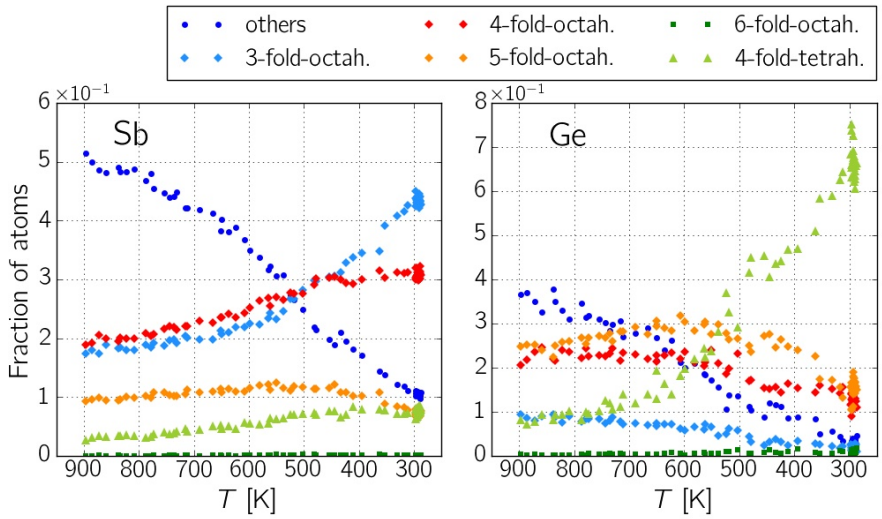

Fig. S12. *Fractions of atoms centered in the different local bonding motifs in terms of the total number of atoms of the corresponding species. Displayed are the curves obtained from AIMD trajectories of the melt-quenching of $Ge_{15}Sb_{85}$, separated by species.*

The results obtained for AIST, resolved by the contributing species, are depicted in Fig. S13. First considering the graphs plotted for the majority species Sb and Te, clear trends regarding the defective octahedral motifs are visible. The fraction of 3- and 4-fold defective octahedra increases for both Sb- and Te-centered motifs, whereas the evolution of the 5-fold defective octahedra contribution is converse, though weak in the case of Te. The 6-fold octahedral and tetrahedral contributions from both Sb and Te atoms are relatively small and stay below 10% during the melt-quenching. Again, the reduction of the number of atoms in a coordination apart from the categories (defective) octahedral and tetrahedral, termed 'others', underlines the increase of order upon cooling. In AIST, the 4- and 5-fold defective octahedra dominate with about 60% contribution for Sb compared to the situation in $Ge_{15}Sb_{85}$ where the 3- and 4-fold defective octahedra accumulating to about 3/4 of the Sb atoms are predominant. Possible signs of structural transition in the evolution of the different bond motifs are less pronounced than seen above for the melt-quenching of $Ge_{15}Sb_{85}$. Referring to the observation of a transition at around 660 K and comparing to the indicators of structural transition observed in the case of $Ge_{15}Sb_{85}$, possible signs of a transition are visible in the curves of Sb and Te. The 4- and 5-fold octahedra curves of Sb reveal points of inflection in the temperature range between 600 K and 700 K, the growth of the number of 3-fold Sb-octahedra accelerates here. Points of inflection can also be observed in this temperature interval in the 3- and 4-fold defective octahedra curves. Furthermore, the number of 5-fold defective octahedra is almost constant above 660 K but starts dropping slightly below it. Turning to the minority species now, the variations of the data points are larger due to the smaller number of Ag and In atoms (both less than 4%) in our AIST composition. The non-ordered Ag atoms show the largest contribution, though decreasing, which is approached upon melt-quenching only by the fraction of 5-fold defective Ag-octahedra. These two contributions accumulate to about 80% of all Ag atoms. The fractions of 4-fold defective Ag octahedra and tetrahedra increase weakly and reach about 10% each at room temperature. 3-fold defective and 6-fold Ag octahedra contribute only weakly. For the fractions of In atoms, we observe a decrease of 3- and 4-fold defective octahedra. Contrarily, 5-fold defective and tetrahedral coordination is enhanced and accumulates to ca. 70% after melt-quenching. The

number of 6-fold octahedra increases, too, but amounts to less than 5% of all In atoms. The number of non-ordered atoms drops from 50% to 10%. Overall, we see stronger fluctuations than observed for the case of Ag. Indicators for a structural transition in the vicinity of 660 K are also present for the minority species. Regarding Ag, the number of atoms categorized as 'others' begins to decrease significantly between 700 and 600 K. Correspondingly, the fraction of 5-fold defective Ag octahedra starts to increase. Other possible trends suffer from weak statistics. Although the data points plotted for In-centered motifs show stronger fluctuations, signs of a structural transition are also visible here: 3- and 4-fold defective In octahedra reduce their contribution starting from a temperature slightly above 600 K downwards, both the strong increase of 5-fold defective In octahedra and the significant increase of In tetrahedra begin between 700 and 600 K. Interpretations of a few single curves might not seem to be a reliable source for the conclusion of a structural transition. However, the fact that we observe changes of the bond coordination upon melt-quenching in most of the different evolution curves for both $Ge_{15}Sb_{85}$ and AIST at the respective transition temperatures found in our experiments and the further analysis of AIMD trajectory data support the conclusion of a connection.

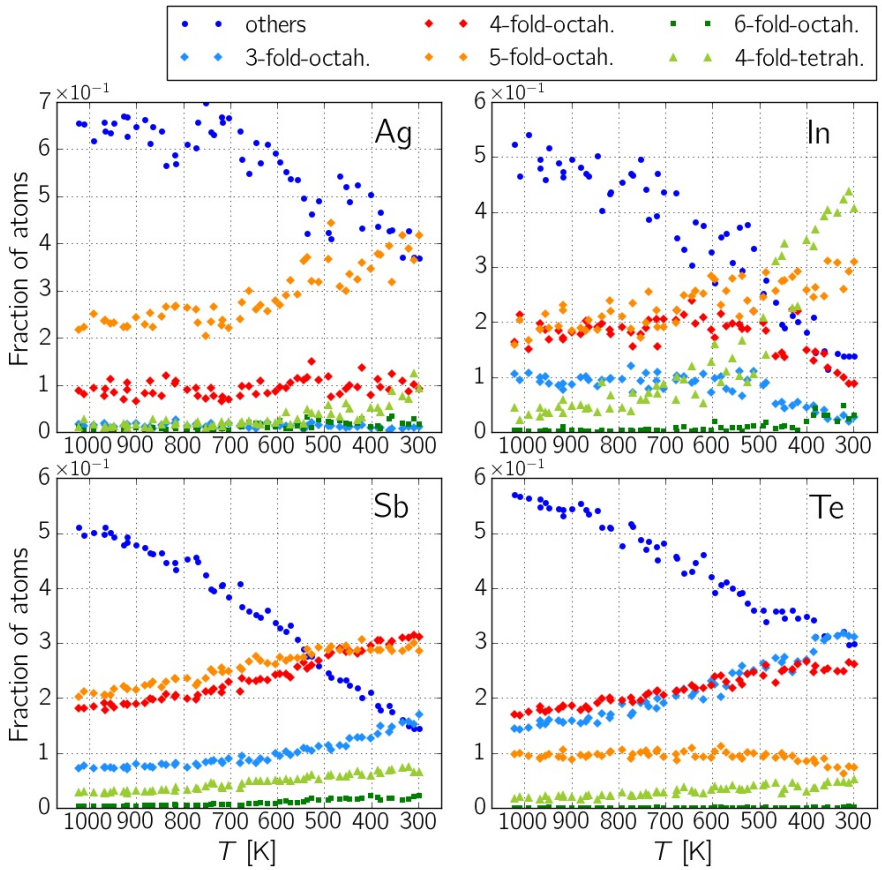

Fig. S13. *Fractions of atoms in the different local bonding motifs in terms of the total number of atoms of the corresponding species. Displayed are the curves obtained from AIMD trajectories of the melt-quenching of AIST, separated by species.*

Bond angle distributions (BADs):

In addition to the structural properties discussed so far in this supplement, being functions of the inter-particle distance, we calculate bond-angle distributions (BADs). Again, bonds are identified applying the cutoffs listed in Table S2. The sections selected from the AIMD trajectory, and therefore the temperature sets, are the same as those analyzed with respect to the structure factors. The families of curves plotted in Fig. S14 to S16 correspond to temperatures averaged over 2,500 MD steps (5 ps) from the respective sections and are depicted with colors ranging from yellow to black representing the cool down from highest to lowest temperature along the melt-quenching trajectory. In case of $Ge_{15}Sb_{85}$, shown in Fig. S14, we observe a shift of the main peak from about 90° to 95° during melt-quenching in the total BAD. The Sb-resolved contribution to the total BAD only shows a less pronounced shift of the central peak from ca. 90° to slightly larger bond angles, whereas the contribution from Ge-centered atom triples results in a main peak which moves more heavily from around 100° to about 109° upon melt-quenching. The latter observation is indicative of considerable and even increasing tetrahedral coordination of Ge atoms in the melt-quenching of $Ge_{15}Sb_{85}$. The main maximum of the Sb-BAD stays close to 90°, indicating that Sb retains its octahedral coordination throughout the melt-quenching. This conclusion is supported furthermore by the transformation of the shoulder above 140° at highest temperature into a local maximum at about 160° at room temperature, an indicator of almost aligned atom triplets. No pronounced local maximum was observed in the BAD of Ge in the large bond angle region since Ge prefers tetrahedral coordination. Shoulders close to 60° present in all three BADs vanish upon melt-quenching. Overall, the BADs get narrower following the trends of enhanced (defective) octahedral and tetrahedral ordering. The situation looks similar for the melt-quench process of AIST. Considering the total and the BADs of the majority species Sb and Te displayed in Fig. S15, we see that the main peaks have bond angles around 90° throughout the melt-quench, without any apparent trend of shifting. The shoulders at about 60° almost vanish. The Sb contribution develops a local maximum above 160° from the shoulder in the range of large bond angles. The shoulder of the Te BAD gets lower and almost becomes a plateau upon cooling. Both the maximum and the shoulder support the existence of almost aligned chains of atoms in AIST. Altogether, the predominant coordination of AIST is therefore octahedral. Since the total BAD does not display any indication of tetrahedral order, contributions to the BAD from Ag and In, depicted in Fig.S8c, do not disturb the overall octahedral coordination noticeably. Although the minority species amount to less than 7% of the number of atoms, we calculate the corresponding BADs for the sake of completeness and to estimate the influence on the total BAD directly. First of all, the limited number of minority atoms results in bad statistics and trends are therefore difficult to recognize from the minority BADs. The contribution to the Ag BAD around 60° decreases and forms a shoulder at lowest temperature. Around 90°, the main peak raises but the distribution stays comparably broad even at room temperature. The BAD of In reveals a significantly narrower main maximum even at largest temperature, centered at around 95°. Its position shifts first to a lower bond angle of about 90° at approximately 530 K and then shifts in the opposite direction again, before reaching an angular value of around 100° at room temperature. The latter peak position is indicative of a considerable fraction of In atoms in tetrahedral coordination at lowest temperature. The preference of In to form tetrahedra does not significantly affect the aforementioned octahedral character of AIST during melt-quenching because of the small number of In atoms in our model.

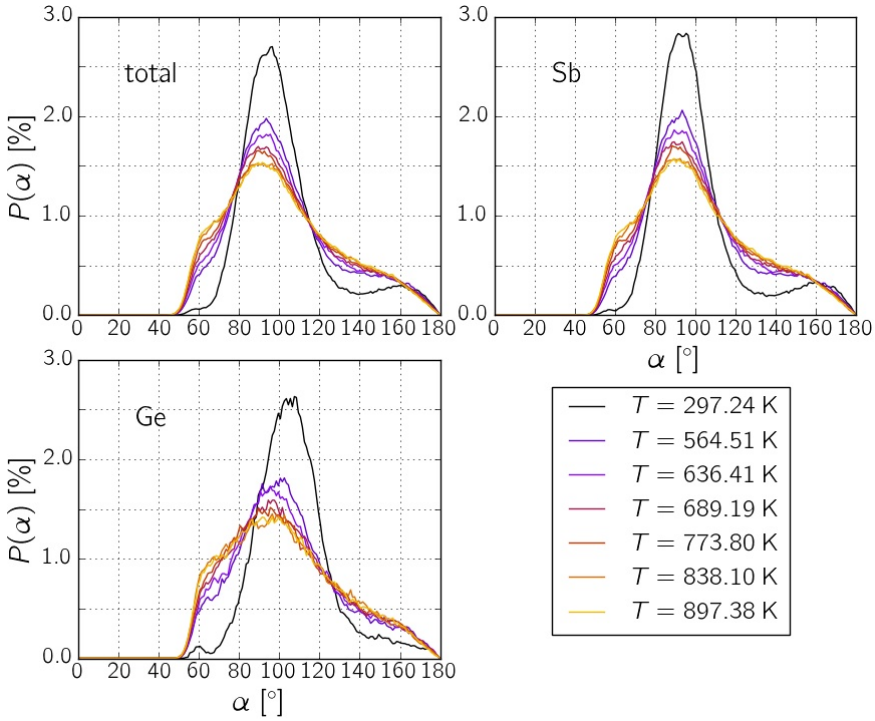

Fig. S14. *Total and species-centered bond angle distributions of melt-quenching $Ge_{15}Sb_{85}$. The temperatures correspond to the ones of the structure factor comparison from Fig. S6, left subplot.*

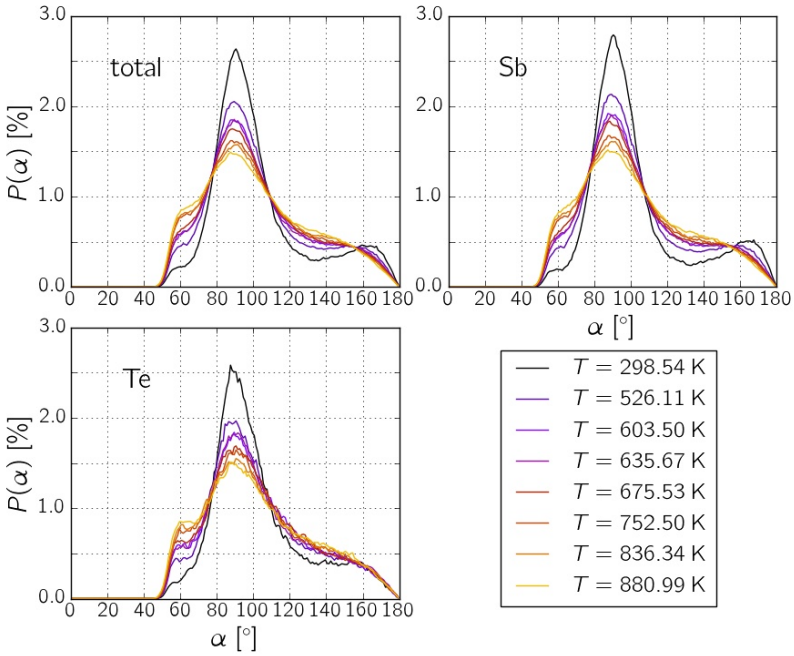

Fig. S15. *Total and majority-species-centered bond angle distributions of melt-quenching AIST. The temperatures are the same as in the structure factor comparison from Fig. S6, right subplot.*

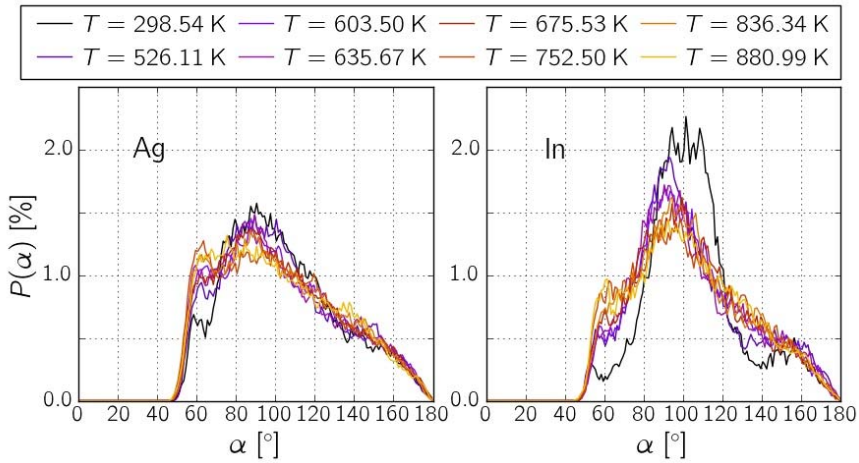

Fig. S16. *Minority-species-centered bond angle distributions of melt-quenching AIST corresponding to the total and majority-species-centered distributions displayed in Fig. S15.*

Nearest neighbor histograms:

In addition to the analysis of the bond-specific structural properties presented above, we investigate distributions of the nearest neighbor distances in the following. For each of the $N_{\mathrm{nb}} = 6$ nearest neighbors of an atom, we establish a histogram which records its distance to the reference atom. Averaging over all atoms in the cell and the 2,500 MD frames (5 ps) of the respective AIMD trajectory section gives the nearest neighbor histograms displayed in Figs. S9a) to S9f) as function of melt-quenching temperature. The AIMD sections are the same selection already used to calculate the structure factors of Fig. S6. The melt-quenching evolution of the total nearest neighbor histograms of $Ge_{15}Sb_{85}$ is shown in Fig. S17 and results for the temperature sets of 897 K and 297 K are also part of Fig. 5 in the main text. There is one subplot for each nearest neighbor order. Histograms for different temperatures are distinguished by curve color, starting with yellow at highest and ranging down to black at lowest temperature. Of course, the centers of the histogram groups shift to larger distances with increasing nearest neighbor order. While the first nearest neighbor histograms concentrate at distances to the reference atom of about 2.8 Å, the sixth nearest neighbor histograms are peaked at distances larger than 3.5 Å. Overlaps between histograms of different orders are obvious. However, the most interesting feature of the total nearest neighbor histograms of $Ge_{15}Sb_{85}$ for our study is the movement of the narrowing peaks of the orders 1, 2, and 3 to shorter distances while fourth, fifth, and sixth order peaks retain their width and move to wider distances. This gives a clear separation into two 3-member groups upon melt-quenching that indicates the onset of Peierls-distortion. The aforementioned main feature of the total nearest neighbor histogram is reproduced to full extent by the contributions from nearest neighbors of Sb, the Sb nearest neighbor histograms depicted in Fig. S18. The contribution from Ge nearest neighbors, as shown in Fig. S19, is responsible for low temperature shoulders and local maxima of the first to fourth order histograms at distances lower than the positions of the main peaks. Furthermore, the partial histograms of Ge at room temperature reveal a 4+2 grouping of nearest neighbor orders rather than the 3+3 grouping of the Sb histograms. This separation is indicative of tetrahedrally coordinated Ge atoms.

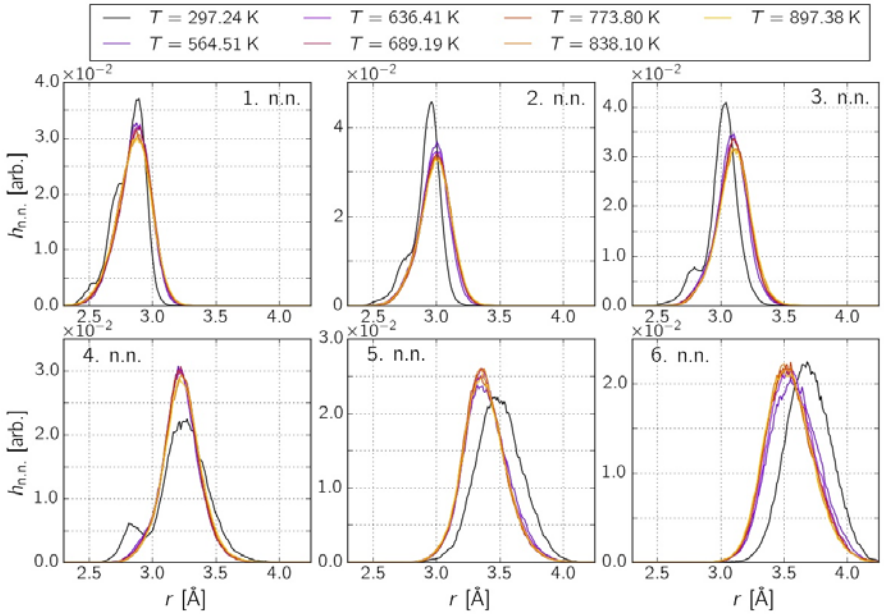

Fig. S17. *Total nearest-neighbor histograms of $Ge_{15}Sb_{85}$ as obtained from analysis of AIMD melt-quenching trajectory sections. These sections are the same as those analyzed to obtain the structure factors in Fig. S6, left side.*

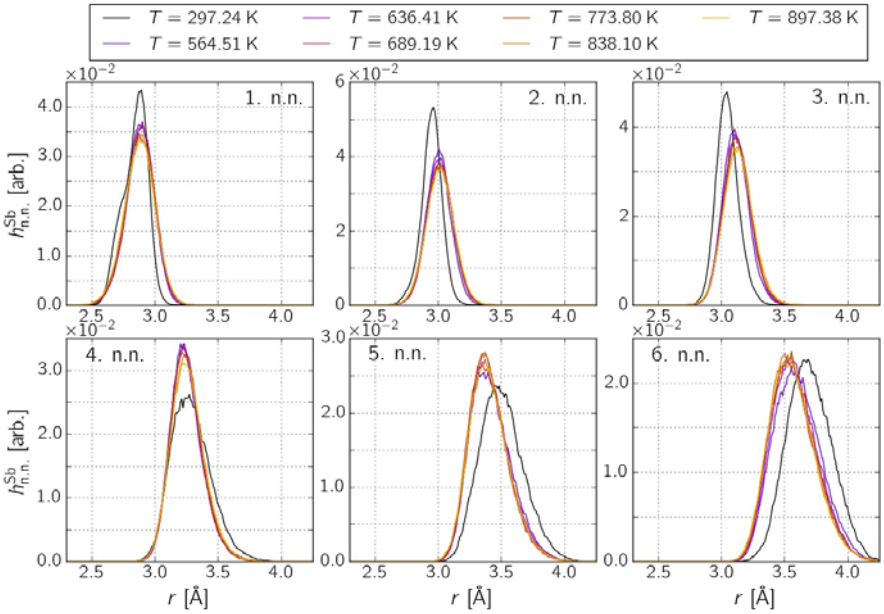

Fig. S18. *Sb-centered nearest-neighbor histograms of melt-quenching $Ge_{15}Sb_{85}$. These distributions give the major contribution to the corresponding total distributions shown in Fig. S17.*

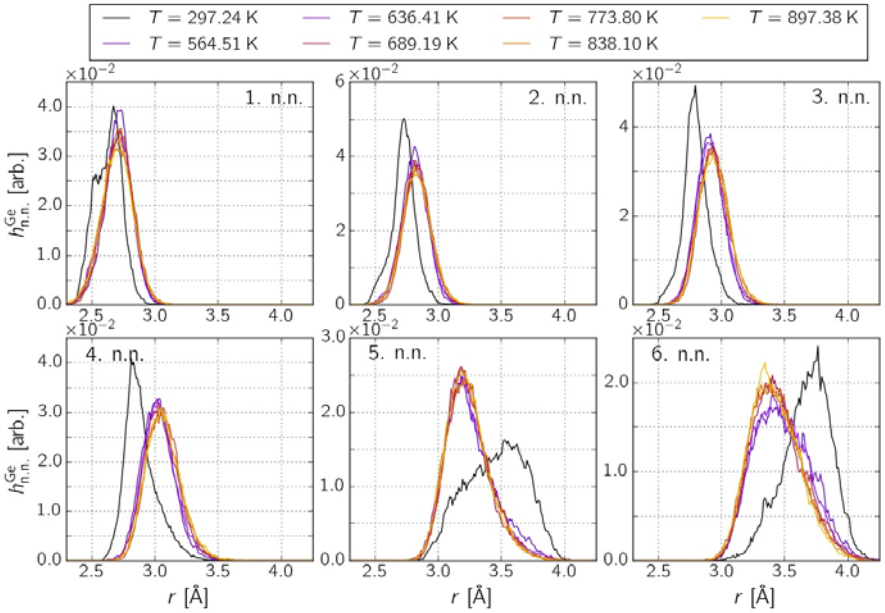

Fig. S19. *Ge-centered nearest-neighbor histograms of melt-quenching $Ge_{15}Sb_{85}$. Together with the distributions displayed in Fig. S18, they give a comprehensive picture of the local structural changes upon melt-quenching.*

The situation observed in case of AIST upon melt-quenching is similar. Again, it is self-evident that the higher the nearest neighbor order of the histogram, the larger becomes the distance at which the histogram is centered. In agreement with our observation for $Ge_{15}Sb_{85}$, we get a pronounced 3+3 splitting for the total nearest neighbor histograms of melt-quenching AIST when cooling down the system to room temperature, as shown in Fig. S20. The peaks of the first three orders become increasingly narrow and higher, whereas the width of the fourth to sixth order is almost conserved, but the height reduces. However, due to a slight left-shift and increasing width at room temperature, the trend of the fourth order peak is less clear compared to the one obtained for $Ge_{15}Sb_{85}$. The shapes of the histograms depicted for nearest neighbors of Sb in AIST in Fig. S21 are even closer to the ones of the total histograms than seen above for the case of $Ge_{15}Sb_{85}$. The important feature of peak separation, indicating Peierls-distortion, is similarly pronounced in both total and Sb nearest neighbor histograms. However, the maxima of the Sb histograms are higher throughout the melt-quenching process for almost all orders. The origin of this difference is to be found in the nearest neighbor histograms of Te, Fig. S22. Here, a 2+4 splitting is dominant, appended by a weaker 3+3 separation: the first and second maxima move to shorter distances, the third one changes weakly only in its shape, and starting from the fourth order, the peaks shift to larger distances upon melt-quenching. Te amounts to about 27% of the atoms in our AIMD model and, as the comparison between total and Sb nearest neighbor histograms shows, does not alter the octahedral character or the trend of increasing Peierls-distortion upon melt-quenching AIST. An effect from the minority species Ag (with 3.7%) and In (with 3%) is not possible as well.

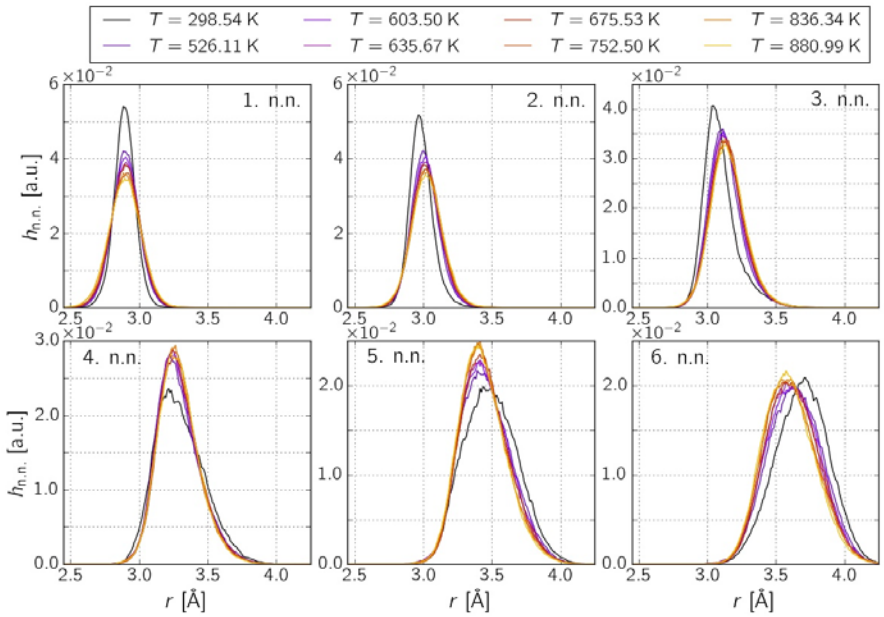

Fig. S20. *Total nearest-neighbor histograms of AIST as obtained from analysis of AIMD melt-quenching trajectory sections. These sections are the same as those analyzed to obtain the structure factors in Fig. S5, right side.*

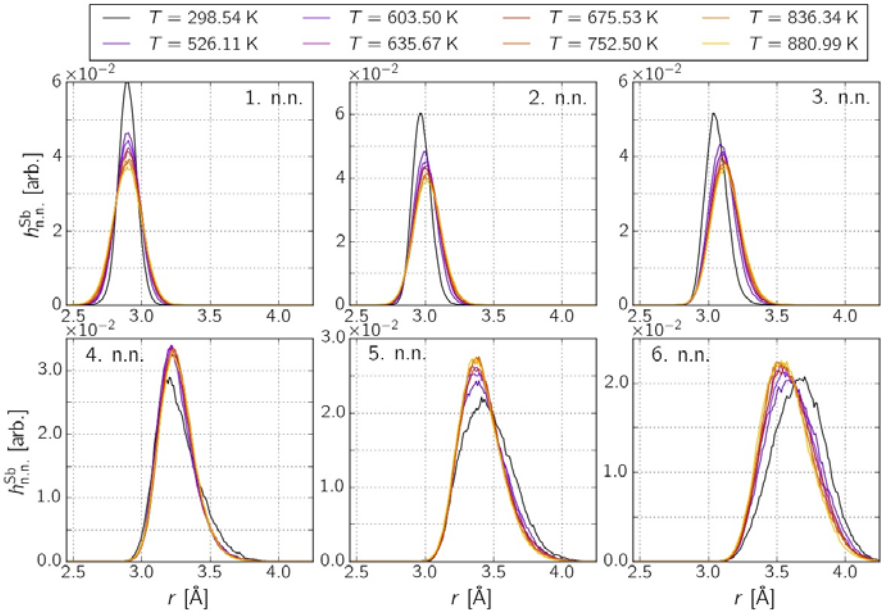

Fig. S21. *Sb-centered nearest-neighbor histograms of melt-quenching AIST.*
These distributions give the major contribution to the corresponding total distributions shown in Fig. S20.

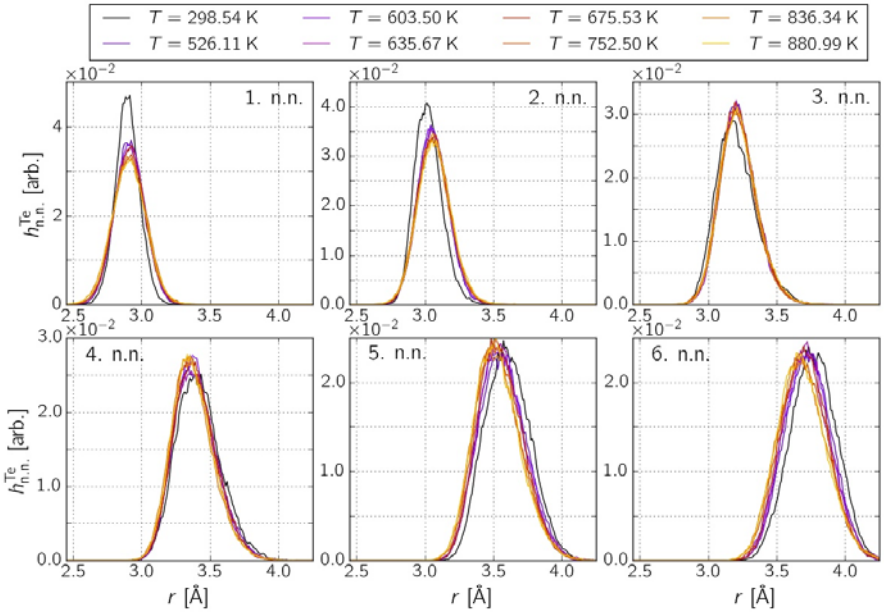

Fig. S22. *Te-centered nearest-neighbor histograms of melt-quenching AIST. Together with the distributions displayed in Fig. S21, the majority species contributions to the local structural changes upon melt-quenching are covered.*

Angular-limited three-body correlations (ALTBCs):

The correlation functions discussed so far in this supplement deal with one-dimensional properties. In order to elucidate possible correlations between structural properties directly, we are dependent on two-dimensional correlation functions. As such, a spatial three-body distribution provides us with the ability to shed light on possible correlations between inter-particle distances in the system under consideration. Restricting the angle separating the two distance vectors from a straight line to an upper limit customizes the (unrestricted) three-body correlation function to the *angular-limited three-body correlation* (ALTBC) function. The ALTBC reveals possible correlations between two almost aligned distance vectors (or bonds, respectively). A schematic of a bond configuration captured by the ALTBC is displayed in Fig. S23. $\vartheta_{lim} = 25°$ is the limiting angle parameter and r_{AB} and r_{BC} are the inter-particle distance variables of the two-dimensional symmetric distribution.

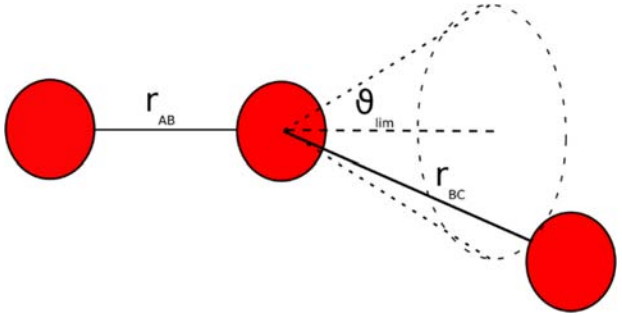

Fig. S23: *Schematic of an atom triple taken into account by the ALTBC function.*

The ALTBCs are averaged over all atomic triplets and the selected AIMD sections of 2,500 (5 ps) length each. Local maxima of the ALTBC outside the main diagonal indicate almost aligned,

alternating short and long inter-particle distance vectors which are considered as bonds if they match the cutoffs from Table S2. The resulting species concentrated ALTBCs of melt-quenching $Ge_{15}Sb_{85}$ for both the liquid and the amorphous phase are depicted in Fig. S24. The subplots on the left are the same as those displayed in Fig. 5e&f of the main text except for the color scales which are fixed between the two temperatures to simplify the investigation of the ALTBC evolution. At a temperature of about 900 K, both distributions display a single broad peak with connected arms along the plot axes. The maxima split into two clearly separated peaks each, line-like distortions indicated by their positions ($r_{AB}^{max}, r_{BC}^{max}$), with $r_{AB}^{max} \neq r_{BC}^{max}$. The peaks of the Sb-centered ALTBC correlate distances of ca. 2.9 and 3.3 Å which are in the wider range bond lengths specified by the cutoff values of Sb bonds. Therefore, the peak separation supports the conclusion of enhancing Peierls distortion. In the case of the Ge-centered ALTBCs, however, we obtain correlated distances of 2.7 and 3.9 Å. The shorter distance corresponds to a bond, whereas the longer distance is far beyond the cutoffs specified in Table S2 for Ge bonds. This observation agrees with the tendency of Ge to form tetrahedra in $Ge_{15}Sb_{85}$ and other PCMs(*48*) upon melt-quenching. Since two bonds from a (Ge-centered) tetrahedron are far from being aligned, they do not contribute to the ALTBC distributions. The value of 3.9 Å found here corresponds to the distance vector between a Ge and a second order shell atom, in alignment to a bond of 2.7 Å length.

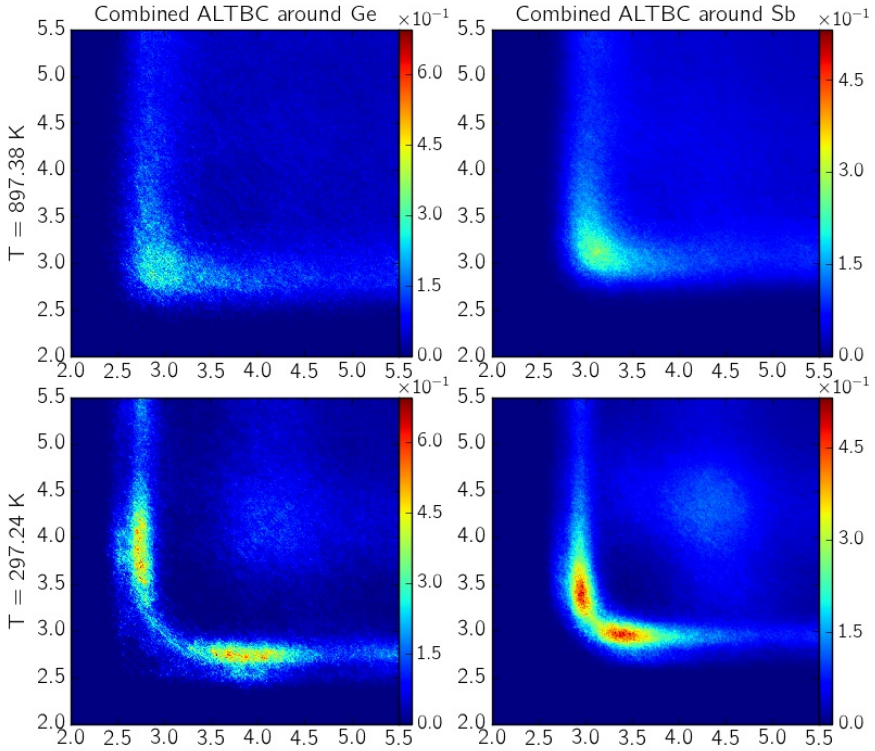

Fig. S24. *Ge- and Sb-centered ALTBC functions of $Ge_{15}Sb_{85}$ in the liquid (upper row) and amorphous (melt-quenched, lower row) phase as obtained from AIMD simulations.*

The initial shape of the Sb-concentrated ALTBC of AIST in the liquid phase looks like the one obtained for $Ge_{15}Sb_{85}$. The melt-quenched AIST, however, does not show two clearly separated maxima, but a broad 'L-shaped' peak. The consequence is that inter-particle distances in the range between about 3.0 and 3.5 Å are significantly inter-correlated. Most distances from this

range fall below the cutoff of 3.4 Å specified in Table S2 and correspond to bonds. The Peierls distortion separates short and long bonds less strictly but it is still a pronounced feature of the Sb-centered ALTBC in melt-quenched AIST. The Te-centered ALTBC displays a clear split-up into two peaks corresponding to inter-correlated distances of about 2.9 and 3.5 Å. Both distances lie in the wider range of the cutoffs from Table S2. However, since its tail ranges to distances significantly above the bonding cutoffs, a relatively large portion of the peak does not contribute to the Te bonds. Collecting contributions from both Sb and Te, the ALTBC distributions indicate a pronounced onset of a Peierls distortion upon melt-quenching AIST.

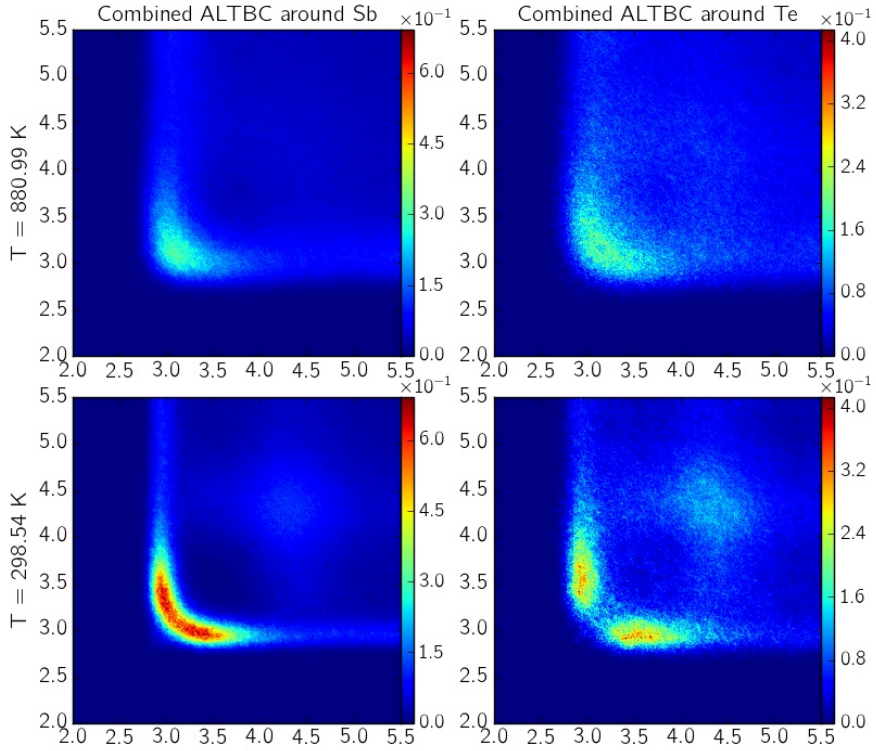

Fig. S25. *Majority-species-centered ALTBC functions of AIST in the liquid (upper row) and amorphous (melt-quenched, lower row) phase as obtained from AIMD simulations.*

Electronic density of states (DOS):

In addition to the analysis of structural properties, a qualitative evaluation of the electronic properties is given in the following. Average electronic density of states (DOS) of $Ge_{15}Sb_{85}$ and AIST are calculated along the melt-quenching AIMD trajectory. For a set of temperatures ranging between the liquid via the supercooled liquid down to the amorphous phase, AIMD configurations have been extracted from the melt-quenching trajectory and carefully equilibrated at the respective temperatures listed in the legends of Figs. S11a&b. Sets of 20 MD frames each have been extracted from AIMD production runs performed for the single temperatures. The DOS have been calculated for the single frames from these sets by means of optimization of the electronic degrees of freedom and averaged over the single-frame DOS results. The resulting averaged total and projected DOS of melt-quenching $Ge_{15}Sb_{85}$ are depicted in Fig. S26. Apparently, a pseudo-gap opens in the total DOS in the vicinity of the Fermi level, with

contributions (lower row of Fig. S26) from both the Sb- and Ge-projected DOS according to the Ge and Sb share of atoms in the model. The total DOS is represented with an additional zoom-in plot to elucidate its evolution upon melt-quenching in detail. A significant opening of the pseudo-gap is visible here from ca. 730 K downwards. The evolution of the total DOS is essentially the same in the case of melt-quenching AIST, as shown in Fig. S27. The onset of the pseudo-gap becomes apparent from about 750 K down to lower temperatures. The pseudo-gaps evolving in $Ge_{15}Sb_{85}$ and AIST both amount to about 50% of the respective high temperature level of the DOS at Fermi level.

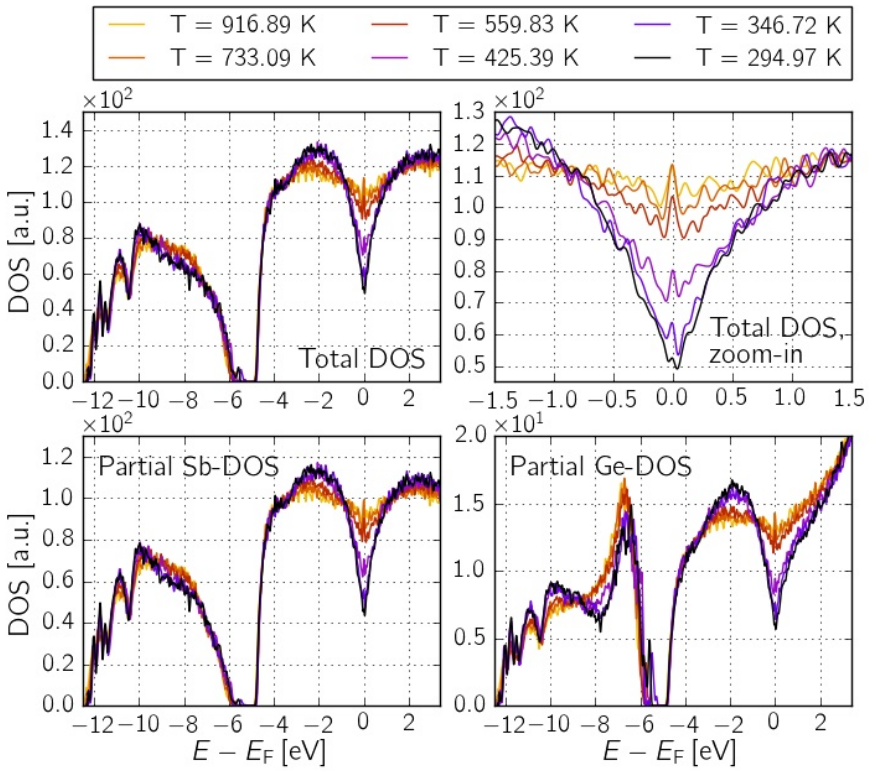

Fig. S26. *Average electronic density of states (DOS) of $Ge_{15}Sb_{85}$ along the melt-quenching AIMD trajectory.*

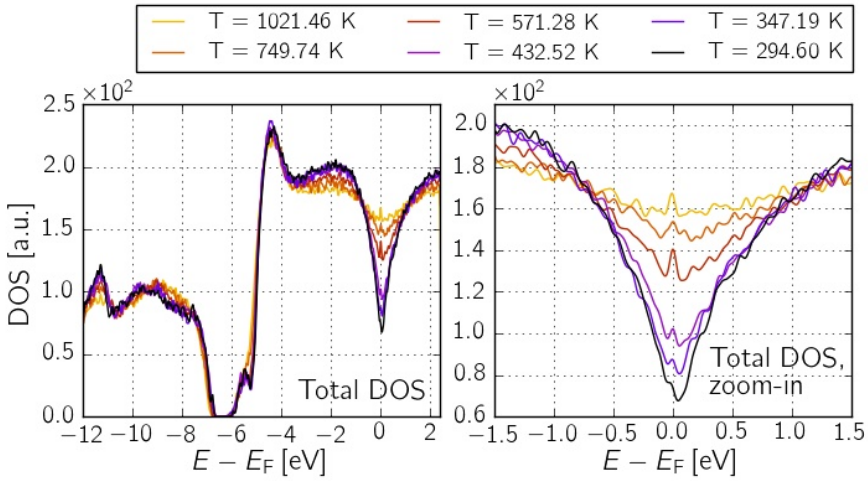

Fig. S27. *Total electronic density of states (DOS) of AIST along the melt-quenching AIMD trajectory, wide energy range and zoom-in plot.*